Climate Response at the Paleocene–Eocene Thermal Maximum to Greenhouse Gas Forcing—A Model Study with CCSM3

A. WINGUTH

The University of Texas at Arlington, Arlington, Texas

C. SHELLITO

University of Northern Colorado, Greeley, Colorado

C. SHIELDS

National Center for Atmospheric Research, Boulder, Colorado

C. WINGUTH

The University of Texas at Arlington, Arlington, Texas

(Manuscript received 4 March 2009, in final form 20 August 2009)

ABSTRACT

The Paleocene–Eocene Thermal Maximum (PETM; 55 Ma) is of particular interest since it is regarded as a suitable analog to future climate change. In this study, the PETM climate is investigated using the Community Climate System Model (CCSM3) with atmospheric CO_2 concentrations of 4×, 8×, and 16× the preindustrial value.

Simulated climate change from 4× to 8× atmospheric CO_2 concentration, possibly corresponding to an environmental precursor of the PETM event, leads to a warming of the North Atlantic Ocean Intermediate-Water masses, thus lowering the critical depth for methane hydrate destabilization by ~500 m. A further increase from 8× to 16×CO_2, analogous to a possible massive methane hydrate release, results in global oceanic warming and stratification. The increase in the radiative surface warming, especially at high latitudes, is partially offset by a decrease in the ocean heat transport due to a reduced overturning circulation. Surface temperature values simulated in the 16×CO_2 PETM run represent the closest match to surface temperature reconstructions from proxies for this period.

Simulated PETM precipitation, characterized by a slight northward shift of the intertropical convergence zone, increases at higher CO_2 concentrations, especially for the northern midlatitudes as well as the high latitudes in both hemispheres. Data-inferred precipitation values and gradients for North America and Spain, for instance, are in good agreement with the 16×CO_2 simulation. Increasing atmospheric CO_2 concentrations might also have favored the release of terrestrial methane through warmer and wetter conditions over land, thus reinforcing the greenhouse gas concentration increase.

1. Introduction

Superimposed on a long-term warming trend from the late Paleocene through the early Eocene is a prominent global hyperthermal at the Paleocene–Eocene boundary (55 Ma), referred to as the Paleocene–Eocene Thermal Maximum (PETM). Surface temperatures increased by 5°C in the tropics (Tripati and Elderfield 2005; Zachos et al. 2005) and midlatitudes (Wing et al. 2005) and by 6°–8°C in the Arctic and sub-Antarctic (Kennett and Stott 1991; Thomas et al. 2000; Sluijs et al. 2006; Hollis et al. 2009) and deep-sea temperatures increased by 4°–6°C (Tripati and Elderfield 2005) relative to Paleocene temperatures (see Fig. 1). At the same time, global humidity and precipitation patterns changed (Robert and Kennett 1994; Wing et al. 2005; Pagani et al. 2006a; Brinkhuis et al. 2006; Sluijs et al. 2008a), as well as

Corresponding author address: Arne Winguth, Department of Earth and Environmental Sciences, The University of Texas at Arlington, 500 Yates St., Arlington, TX 76019.
E-mail: awinguth@uta.edu

DOI: 10.1175/2009JCLI3113.1

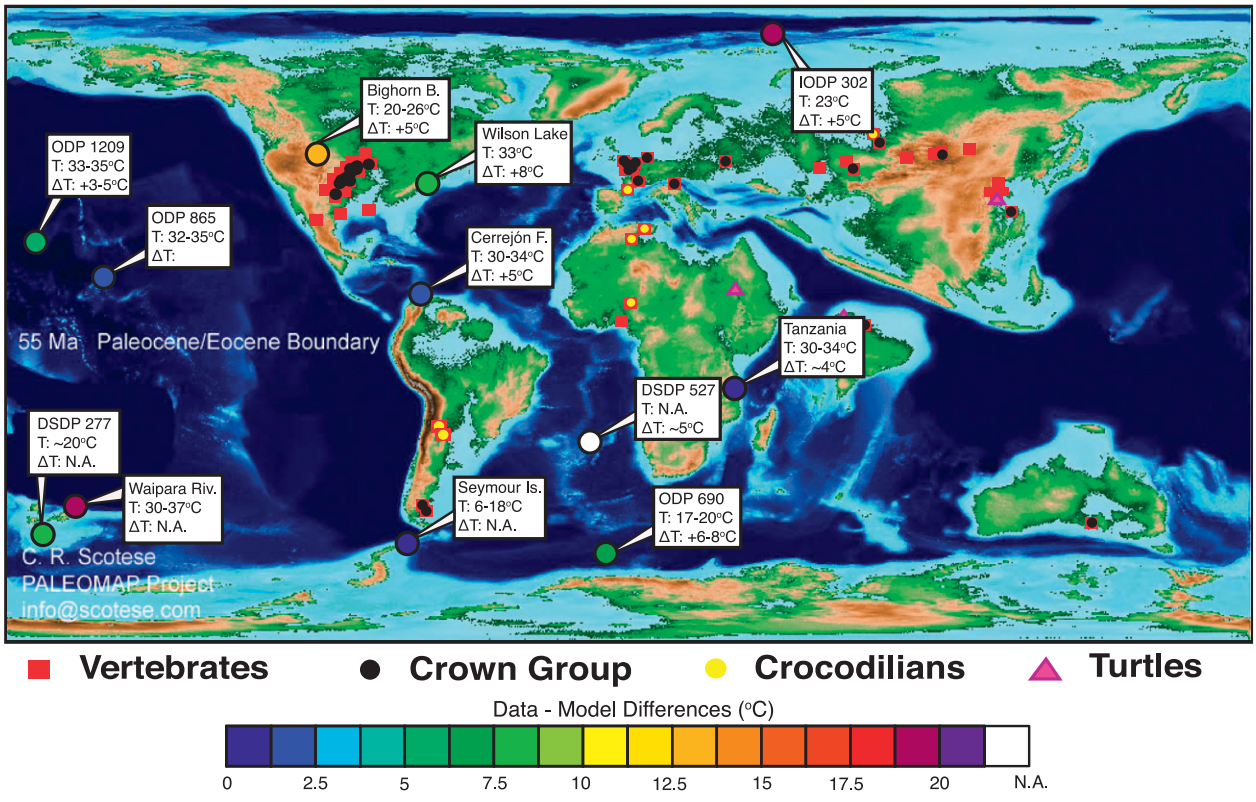

FIG. 1. Geographical reconstruction for the PETM from the PALEOMAP Project (see www.scotese.com). Boxes indicate reconstructed surface temperatures across the Paleocene–Eocene boundary and temperature anomalies relative to Paleocene background temperatures (Shackleton and Kennett 1975; Thomas et al. 1999; Wing et al. 2005; Tripati and Elderfield 2005; Bralower et al. 2006; Zachos et al. 2004, 2006; Sluijs et al. 2006, 2007b, 2008a; Pearson et al. 2007; Ivany et al. 2008; Hollis et al. 2009). Filled circles denote differences between temperature reconstructions and the 8×CO_2 PETM model simulation. Fossil locations taken from Markwick (1997).

deep-sea circulation patterns (Nunes and Norris 2006; Thomas 2003). The PETM is marked by a major (>3.0 ‰) negative carbon isotope excursion, documented in marine and terrestrial fossils (e.g., Koch et al. 1992; Kelly et al. 1998; Handley et al. 2008), and a worldwide seafloor carbonate dissolution horizon (e.g., Bralower et al. 1997; Lu et al. 1998; Schmitz et al. 1996; Thomas et al. 2000), as well as shoaling of the lysocline and carbonate compensation depth (Zachos et al. 2005). These characteristics are consistent with the release of more than 2000 PgC of isotopically depleted carbon into the ocean–atmosphere system within less than 10 000 years (Zachos et al. 2007, 2008), pointing to a greenhouse gas–driven warming. Hence, the PETM is regarded as a suitable analog for future climate change and carbon uptake and is of particular interest for evaluating the theoretical understanding of the complex processes that govern the interactions between climate and biogeochemical cycles in response to extreme radiative forcing.

The causes for the sudden warming at the Paleocene–Eocene boundary are still controversial. The ^{13}C-depleted carbon (in the form of CO_2 and/or CH_4) may have been injected into the global exogenic carbon pool from the sea floor (Dickens et al. 1995, 1997; Higgins and Schrag 2006; Pagani et al. 2006b) or from wetlands (Pancost et al. 2007). One possible sequence of events consists of relatively rapid bottom-water warming during the Late Paleocene, possibly driven by a volcanism-induced greenhouse gas increase, that triggered a massive release of methane hydrates and thus caused the rapid climate change at the PETM (Sluijs et al. 2007a).

Greenhouse gas sensitivity experiments with atmosphere (Sloan and Rea 1996; Huber and Sloan 1999; Shellito et al. 2003), ocean (Bice et al. 2000; Bice and Marotzke 2002), or coupled atmosphere and ocean (Huber and Sloan 2001; Huber and Caballero 2003; Shellito et al. 2009) general circulation models have been used to simulate the mean climate and its variability during the Eocene, but these studies have not been able to reproduce the high temperatures of the PETM and the early Eocene, nor have they been able to provide insight regarding the cause of this warming.

Here, we use the comprehensive Community Climate System Model version 3 (CCSM3) (Collins et al. 2006a)

to explore the hypothesis that changes in intermediate- or deep-water formation in the subtropics (Kennett and Stott 1991) or at high latitudes (Bice and Marotzke 2002) might have facilitated methane hydrate destabilization. We also assess the response of atmospheric and oceanic dynamics to large changes in radiative forcing at the PETM and compare model output with climate proxies from this time to determine whether an updated model can produce a better match with proxies than previous modeling studies.

2. Model description and forcing

a. CCSM3

The National Center for Atmospheric Research CCSM3 is a global, coupled climate model including the ocean, atmosphere, sea ice, and land surface. Model details are given elsewhere (Collins et al. 2006a; Yeager et al. 2006, and references therein). The atmospheric general circulation model, the Community Atmosphere Model version 3 (CAM3), is a primitive equation model with spectral horizontal resolution of T31, corresponding to an equivalent grid spacing of approximately 3.75° in latitude and longitude and with 26 vertical unevenly spaced terrain-following levels (Collins et al. 2006b). The atmospheric component is connected via the coupler to a land surface model, the Community Land Model (CLM3.0) with a resolution of 2° × 2° (Oleson et al. 2004) and without dynamic vegetation. The land surface model includes a river routing scheme that computes the direction of river runoff at each gridpoint from the orography under the assumption that all rivers drain into the ocean. The ocean general circulation model is the NCAR Parallel Ocean Program version 1.4 (POP1.4), a primitive equation model in spherical polar coordinates with dipole grids resolved horizontally × 3 (100 × 116 points) and with 25 layers in the vertical coordinate (Gent et al. 2006). The sea ice model is a thermodynamic model with subgrid parameterization of ice thickness and elastic viscous rheology (Briegleb et al. 2004; Holland et al. 2006). Its horizontal and vertical resolution is the same as in POP1.4.

b. Paleogeography and vegetation

The PETM geography has been updated from Shellito and Sloan (2006), following Sewall et al. (2000, see Figs. 1 and 2). A prescribed land surface cover with 15 different vegetation types, taken from Shellito and Sloan (2006, supplemental document A available at the Journals Online Web site: http://dx.doi.org/10.1175/2009JCLI3113.s1), is applied. Seaways from the Arctic to the open ocean are not resolved and were therefore closed in previous simulations. Here, a marginal sea parameterization (Smith and Gent 2004) has been introduced for the Arctic Ocean to balance its freshwater fluxes. The amount of excess or deficit of the local freshwater balance over the dynamically active Arctic Ocean is transported to or from the adjacent northeastern Tethys. This parameterization assures that volume-mean salinity of the marginal sea remains constant so that unreasonable salinity values are avoided. Eustatic sea level rise at the PETM may have played an important role in establishing connections between the Arctic and the world oceans (Sluijs et al. 2008b). In this study, the main Arctic exchange of freshwater is assumed to have occurred across the Turgay Strait to the Tethys (e.g., Iakokleva et al. 2001; Brinkhuis et al. 2006). The Bering Strait was probably closed (Lyle et al. 2008; Marincovich and Gladenkov 1999) and the Arctic–Atlantic connection was affected by strong volcanic activity in the North Atlantic Igneous Province (e.g., Maclennan and Jones 2006; Storey et al. 2007, and references therein).

c. Radiative forcing

Consistent with calculations by Boothroyd (see Caldeira and Kasting 1992), a solar constant of 1362 W m^{-2} for the PETM is employed, corresponding to a reduction of the present-day solar constant by 0.44%. The decrease of the earth's rotation rate with time has been estimated from paleontological analysis (Scrutton 1978) and tidal analysis (Williams et al. 1997). However, changes from the PETM to present are smaller than 3% and are neglected in CCSM. As assumed in earlier studies for the Eocene (Shellito et al. 2003; Huber and Sloan 2001), a circular orbit of the earth around the sun (eccentricity = 0) and an obliquity (axial tilt) of 23.5° have been applied. This setting causes an equal receipt of solar insolation for both hemispheres.

Reconstructions of greenhouse gas concentrations [based on carbon isotope excursions and boron isotopes in sedimentary records, e.g., Pearson and Palmer (2000); Yapp (2004); Royer et al. (2007); Zachos et al. (2008) and references therein] indicate PETM atmospheric CO_2 levels within a range of 1000 to 4000 ppmv. Therefore, three sensitivity experiments have been carried out (one with 4, one with 8, and one with 16 times the preindustrial CO_2 level of 280 ppmv). These CO_2 levels correspond to a radiative forcing of about 8.7 W m^{-2} ($4\times CO_2$), 13.1 W m^{-2} ($8\times CO_2$), and 17.5 W m^{-2} ($16\times CO_2$), respectively (Table 1) (Houghton et al. 2001; Ramaswamy et al. 2001). The increase from $4\times CO_2$ to $16\times CO_2$ would have been equivalent to a total injection of 6700 GtC, corresponding to the estimated carbon pulse required to reproduce seafloor carbonate dissolution, as suggested by a modeling study of Panchuk et al. (2008).

d. Initialization of the PETM simulations

The PETM simulations are started from a global temperature and salinity profile derived from a previous

TABLE 1. Results from the PETM CCSM simulations (global and annual averages, unless otherwise noted). For present day (PD), see also Otto-Bliesner et al. (2006). The direct CO_2 radiative forcing at the tropopause is calculated as $F_{CO2} = 6.3 \ln(pCO_2/pCO_{2ref})$ (W m^{-2}) with the preindustrial CO_2 partial pressure pCO_{2ref} = 280 ppmv (see Houghton et al. 1990).

Expt	Atm. CO_2 conc. (ppmv)	Direct CO_2 rad. forcing (W m^{-2})	SAT global (°C)	SAT land (°C)	SST (°C)	Precip. global (mm day^{-1})	Precip. land (mm day^{-1})	A_{ice} (%)
PD	355	1.5	14.14	7.79	19.37	2.71	1.96	26.60
PETM 4×CO_2	1120	8.7	20.97	17.20	22.66	3.18	2.91	3.72
PETM 8×CO_2	2240	13.1	23.45	20.26	24.58	3.33	3.18	0.03
PETM 16×CO_2	4480	17.5	26.23	23.78	27.18	3.49	3.41	0.00

560-yr 8×CO_2 Eocene simulation. CCSM3 is integrated with improved geography (section 2d) for 1500 years for the 4×CO_2, 8×CO_2, and 16×CO_2 simulations. This integration time corresponds to the adjustment time of the radiocarbon tracer in the present-day ocean. The simulated surface climate adjusts after about 200 years, but a small drift remains in the deep sea after 1500 years of integration (see section 4c for model adjustment). For present-day simulations, CCSM3 produces stable climate simulations of millennial duration without ad hoc adjustments to the fluxes exchanged among the component models (see Collins et al. 2006a).

3. Results from PETM simulations (atmosphere)

a. Surface temperature

The effective difference in radiative forcing between the PETM 8×CO_2 and the present-day simulation with CCSM3 [described in Yeager et al. (2006) and Otto-Bliesner et al. (2006) and used hereafter for comparison] amounts to 11.6 W m^{-2} (Table 1). The PETM orbital parameter settings yield a change of solar radiation of 20 W m^{-2} in the northern polar region during summer and a similar negative change in fall, relative to the present-day simulation (Fig. 2). In the Southern Hemisphere, the maximum change relative to the present-day simulation is 30 W m^{-2} for October, and the most negative change is ~−20 W m^{-2} (during January).

Mean global surface temperature for the PETM 8×CO_2 simulation is 23.5°C. The difference between the PETM 8×CO_2 simulation and the present-day simulation is 9.3°C, and the respective differences between 8×CO_2 and 4×CO_2 and between 16×CO_2 and 8×CO_2 are +2.5° and +2.8°C (Table 1). All PETM experiments yield significantly higher zonal average surface air temperatures than the present-day experiment, especially at high latitudes (Fig. 3). The lower than present-day simulated pole-to-equator temperature gradient in a high CO_2 world is consistent with previous studies (e.g., Sloan and Barron 1992; Sloan and Rea 1996; Shellito et al. 2003; Weijers et al. 2007). Mean annual temperatures for the two higher CO_2 simulations are above freezing near the North Pole (4°C for 8×CO_2, 8°C for 16×CO_2) and the South Pole (2°C for 8×CO_2, 6°C for 16×CO_2). Significant differences between the present-day and the PETM simulations are related to higher greenhouse gas concentrations, a reduced ice albedo feedback, lower elevations due to the absence of ice sheets in Antarctica and Greenland (Oglesby 1989), the positions of continents (e.g., a more poleward position of Australia), and associated changes in the ocean currents (see section 4a). Tropical temperatures for the three scenarios are about 30°C (4×CO_2), 32°C (8×CO_2), and 34°C (16×CO_2). The increase in tropical temperature with an increase in the CO_2 radiative forcing predicted in this study contradicts the concept of the thermostat hypothesis (Ramanathan and Collins 1991), which assumes that an enhanced cloud albedo effect with increased greenhouse gas forcing has a stabilizing effect on sea surface temperature [see, e.g., Pierrehumbert (1995) for a detailed discussion]. Recently, warm tropical temperatures of

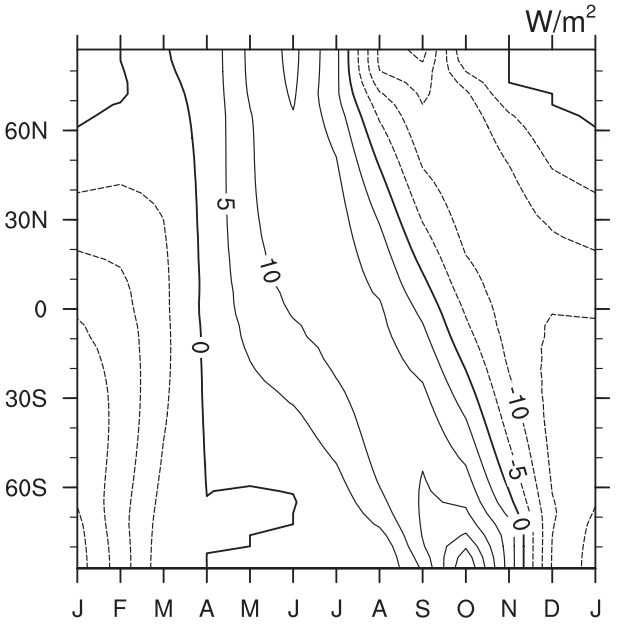

FIG. 2. Difference in incoming solar radiation (W m^{-2}) between PETM orbital configuration (see text) and the present day as a function of month and latitude.

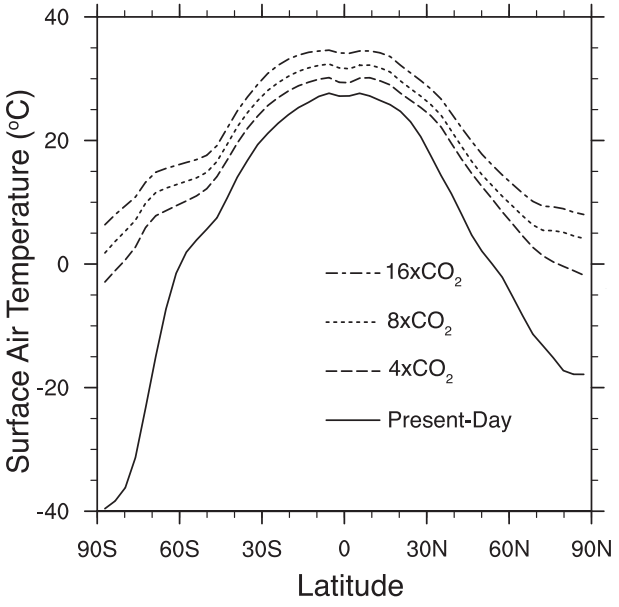

FIG. 3. Zonally averaged (50-yr mean) surface air temperature (°C) for present day (solid), $4\times CO_2$ PETM (long dashed), $8\times CO_2$ PETM (short dashed), and $16\times CO_2$ PETM (dashed–dotted).

30°–34°C for the Late Paleocene (58–60 Myr B.P.) have been inferred from fossil remains of a giant boid snake from the Cerrejón Formation in northeastern Colombia (Head et al. 2009). These findings also suggest that at the PETM and during the early Eocene, tropical temperatures in South America may have been significantly higher than today, in agreement with our model results (Fig. 1 and Table 2, similar to Fig. 1 in Huber 2009).

Maximum temperatures (~50°C for $8\times CO_2$) are simulated over subtropical Africa and South America in all PETM experiments, resulting in warm sea surface temperatures in the adjacent oceans through advection. Over the continents, the 30°C isotherms in the $8\times CO_2$ simulation reach up to 30° latitude, about 5° more poleward than those in the present-day simulation (Fig. 4a). Mean annual surface temperature values simulated for the approximate paleolocation of the Bighorn Basin (Wyoming) are 9.5°C for the $8\times CO_2$ experiment, and 2.4°C cooler and 3.5°C warmer for the $4\times CO_2$ and $16\times CO_2$ experiments, respectively (Figs. 4c,d and Table 2). All simulated temperatures lie below the reconstructed temperatures of 20° to 26°C inferred from leaf margin analysis (Wing et al. 2005) and $\delta^{18}O$ proxies (Fricke and Wing 2004), with the smallest bias reached by the $16\times CO_2$ simulation. The highest maximum surface temperatures are simulated over South America and Africa (Fig. 4b), exceeding 50°C in central South Africa. Simulated minimum surface temperatures ($8\times CO_2$) are between 3° and 7°C over the Arctic and about −10°C over northeast Asia. The Arctic region in the $4\times CO_2$ scenario (Fig. 4c) is up to ~3°C cooler than in the $8\times CO_2$ run, likely due to sea ice albedo effects in winter.

Remarkable temperature increases are simulated for the doubling of CO_2 from $8\times CO_2$ to $16\times CO_2$ of up to 5°C over South America and South Africa and over the Arctic (Fig. 4d). These areas are characterized by high absorbance of solar radiation through warm C_4 grass and savanna-type vegetation, leading to a relatively low latent heat flux (<60 W m^{-2}). In addition, latent heat flux over the ocean is significantly higher in a high CO_2 world (Manabe et al. 1991). Both of these effects contribute to a strong land − sea temperature contrast in these areas, especially in the $16\times CO_2$ simulation. Southern Ocean water masses moderate the climate over the polar Southern Hemisphere so that south of 60° the temperature increase in response to the increase of CO_2 radiative forcing is only ~2.5°–4.5°C.

TABLE 2. Surface temperatures from data and modeled temperatures (annual average as well as summer values, corresponding to a July average in the NH and January average in the SH) for locations shown in Fig. 1 (see also for references). Paleolocations have been calculated using the PointTracker software by C. Scotese.

				Annual average			Summer		
Name	Paleolocation	Data (°C)	Age	$4\times CO_2$ (°C)	$8\times CO_2$ (°C)	$16\times CO_2$ (°C)	$4\times CO_2$ (°C)	$8\times CO_2$ (°C)	$16\times CO_2$ (°C)
DSDP 277	~60.6°S, 170.7°W	~20	~51 Ma	8.1	11.7	14.8	10.8	15.8	19.2
Waipara River	~52.1°S, 160.8°W	30–37	~51 Ma	11.5	14.3	16.7	13.7	18.8	20.8
Seymour Island	~63.4°S, 64.1°W	6–18	~54–53 Ma	7.4	10.9	13.9	11.5	15.5	19.0
ODP 690	~65.7°S, 7.2°W	17–20	PETM	8.4	11.9	15.1	12.7	16.6	19.9
Wilson Lake	~39.7°N, 57.3°W	33	PETM	23.3	25.1	27.5	27.2	29.2	31.4
IODP 302	~81.5°N, 42.6°E	23	PETM	−0.7	3.2	7.2	0.6	6.6	10.8
ODP 865	~8.3°N, 151.4°W	32–35	PETM	30.0	31.6	33.8	30.1	31.8	33.9
ODP 1209	~23.6°N, 171.1°W	33–35	PETM	26.5	28.1	30.5	27.8	29.7	32.2
Tanzania	~19.2°S, 30.9°E	30–34	PETM	28.6	30.9	33.4	30.7	33.0	35.2
Bighorn Basin	~49.0°N, 89.5°W	20–26	PETM	7.1	9.5	13.0	19.3	22.9	28.5
Cerrejón Formation	~8.4°N, 60.0°W	30–34	~58 Ma	29.0	31.2	33.5	29.2	31.4	33.5

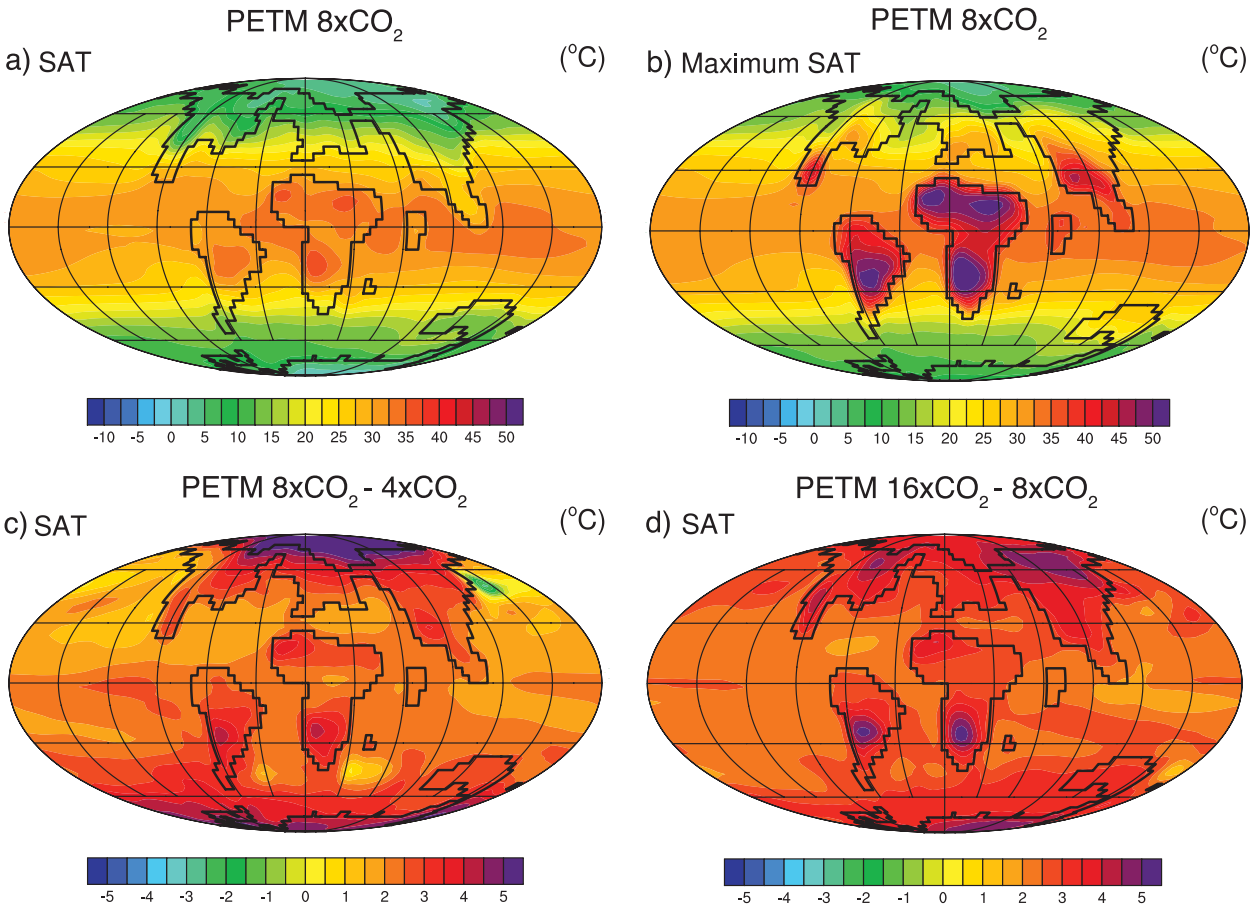

FIG. 4. (a) Surface air temperature (SAT) (50-yr mean), (b) maximum surface air temperature for the $8\times CO_2$ PETM experiment, and temperature differences (c) between the $8\times CO_2$ and $4\times CO_2$ and (d) between the $16\times CO_2$ and $8\times CO_2$ PETM experiments.

b. Vertical temperature

The effect of an increase in greenhouse gas forcing on the vertical temperature structure is expected to be similar to future climate change simulations (Solomon et al. 2007) and previous Eocene simulations (Sloan and Rea 1996). In comparison to the present-day run, the $8\times CO_2$ PETM simulation predicts a warmer troposphere in response to radiative heating (with more intense warming near the surface in the Northern Hemisphere related to its larger land fraction). This simulation also produces a decrease in stratosphere temperatures, associated with a net radiative cooling to space by greenhouse gases. For the $8\times CO_2$ PETM simulation, the maximum increase in the tropospheric temperature relative to present-day is 28.7°C (not shown) in the upper tropical troposphere. With an increase in the atmospheric CO_2 radiative forcing from $4\times CO_2$ to $8\times CO_2$, the maximum upper troposphere temperature in the tropics at ~12-km altitude increases by up to 5.1°C and from $8\times CO_2$ to $16\times CO_2$ by up to 6.1°C. The most significant stratosphere cooling in the $8\times CO_2$ simulation relative to present-day is by 16.6°C in the Arctic at an altitude of ~20 km. The midstratosphere cooling pattern can be linked to the widening of the tropical belt and the enhanced vapor transport into the stratosphere (Seidel et al. 2008). Cooling in the middle stratosphere increases by up to 2.4°C for a CO_2 doubling from $8\times CO_2$ to $16\times CO_2$ and by up to 3.5°C for a CO_2 quadrupling from $4\times CO_2$ to $16\times CO_2$, with maximal differences near 60°S.

c. Precipitation and evaporation

Overall, PETM precipitation slightly increases (and evaporation minus precipitation slightly decreases, Fig. 5) in mid to high latitudes with increased surface temperatures in response to CO_2 radiative forcing (as also inferred by Sloan and Rea 1996 and Shellito et al. 2003). One area with high precipitation sensitivity is the tropical region (Fig. 5), predominantly reflecting the slightly northward-shifted intertropical convergence zone, which is strong for the PETM simulations over the Pacific and Indian Oceans (see Fig. 6 for $8\times CO_2$). The difference in

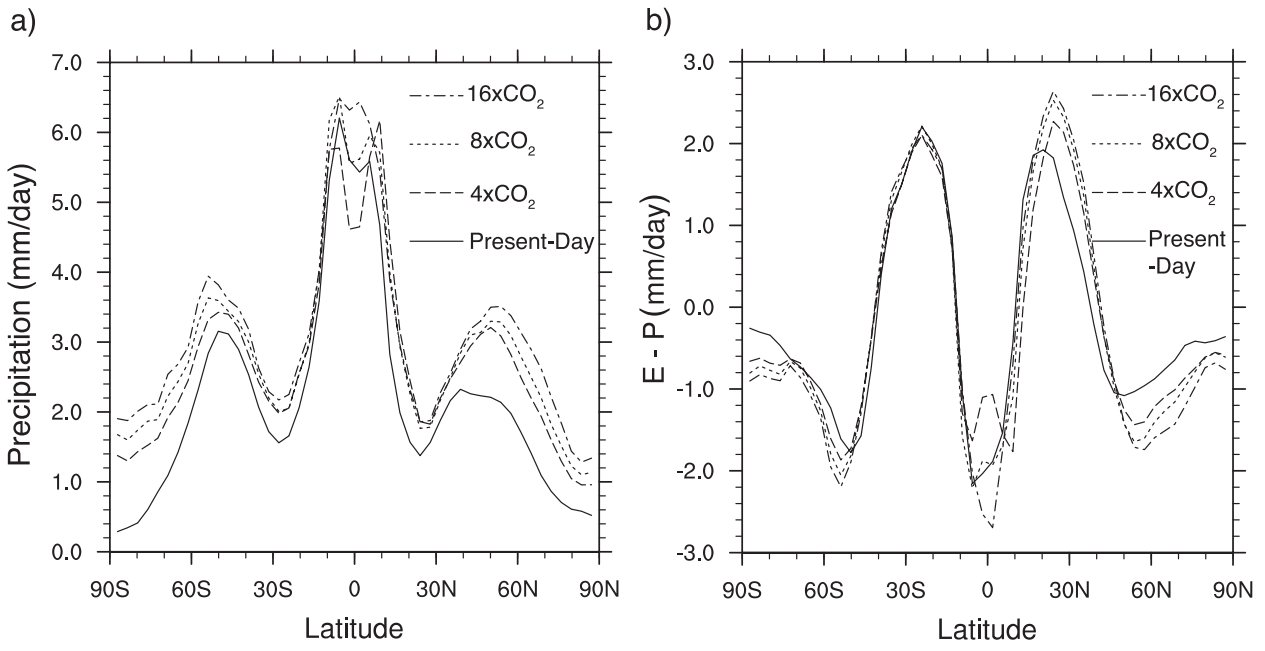

FIG. 5. Zonally averaged (50-yr mean) (a) precipitation (mm day^{-1}) and (b) evaporation minus precipitation (mm day^{-1}) for the present day (solid), 4×CO_2 PETM (long dashed), 8×CO_2 PETM (short dashed), and 16×CO_2 PETM (dashed–dotted).

PETM to present-day precipitation can be attributed to changes in the radiative forcing, vegetation cover, and geography. The geographic effect has been investigated by Barron et al. (1989), who argued that a higher than present-day ratio of tropical land to ocean area, at the PETM, reduces the tropical ocean surface and hence the oceanic source of atmospheric moisture. This significantly reduces not only tropical precipitation but also poleward moisture transport from the tropics.

Sedimentary records from the midlatitudes of the North American continent have produced conflicting evidence for hydrological changes in this region. Based on the assumption of carbon isotope excursion amplification in soil organic matter from Wyoming, also from Spain and China, Bowen et al. (2004) calculated an ~25% increase in relative humidity for the northern continental midlatitudes in order to explain the offset in carbon isotope excursion values between marine and terrestrial records at the PETM. Wing et al. (2005), on the other hand, used vegetation analysis (based on leaf area) for the North American midlatitude location (Bighorn Basin, Wyoming) and inferred a decrease of ~40% in precipitation at the beginning of the PETM (yielding mean annual precipitation values of 41 or 80 cm) and an increase later during the PETM event (yielding mean annual precipitation values of 144 or 132 cm). Recently, Bowen and Bowen (2008) deduced drier PETM conditions for a location in Utah, situated approximately 500 km south of the Wyoming location, and suggested that precipitation was diverted from mid to high latitudes. These findings are, however, controversial since Retallack (2005) reconstructed a precipitation increase for the PETM at a nearby location in Utah, with annual values of 663 ± 147 mm (see also Retallack 2009; Bowen and Bowen 2009). Our study shows a slight increase in precipitation in the midlatitudes with increasing greenhouse gas concentrations from 4×CO_2 to 16×CO_2 (Figs. 5 and 6) but does not explain the significant change in humidity as suggested by Bowen et al. (2004). The simulated precipitation values of ~1–2 mm day^{-1} in the Wyoming area for the 8×CO_2 experiment (Fig. 6a) are at the lower end of the Wing et al. (2005) estimates, whereas the slightly increased values for the 16×CO_2 simulation (Fig. 7b) are in better agreement with these data. For the Utah region, our simulated values in the 8×CO_2 experiment are ~2–3 mm day^{-1} (Fig. 6a). Contrary to the Bowen and Bowen (2008) proposition, the simulated precipitation amounts decrease from lower to higher midlatitudes in North America, mainly owing to monsoonal moisture transport from the south (Mississippi Embayment) during summer [in general agreement with the high-resolution study by Sewall and Sloan (2006)]. A continental record from the Spanish Pyrenees shows evidence for strong increases in seasonal rain at the PETM (Schmitz and Pujalte 2007). Enhanced moisture transport from the Tethys seems to have played a major role at this time, especially during the summer months, as also indicated in our simulations, with growing

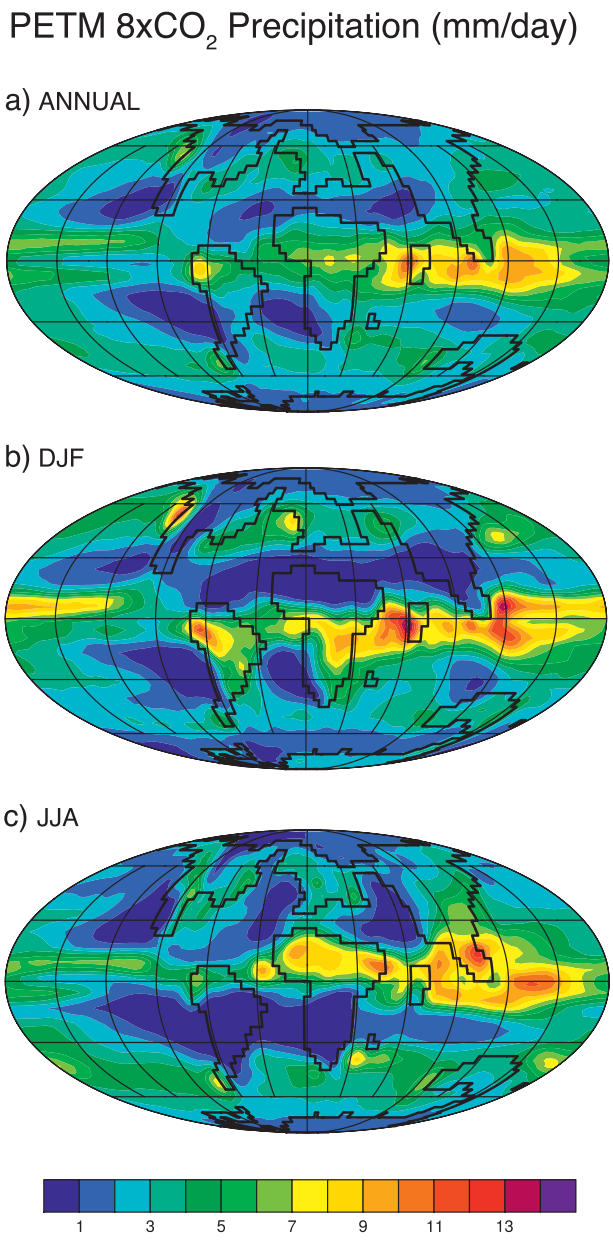

FIG. 6. Precipitation (mm day^{-1}) for the 8×CO_2 PETM experiment (50-yr mean): (a) annual average, (b) NH winter (DJF), and (c) NH summer (JJA).

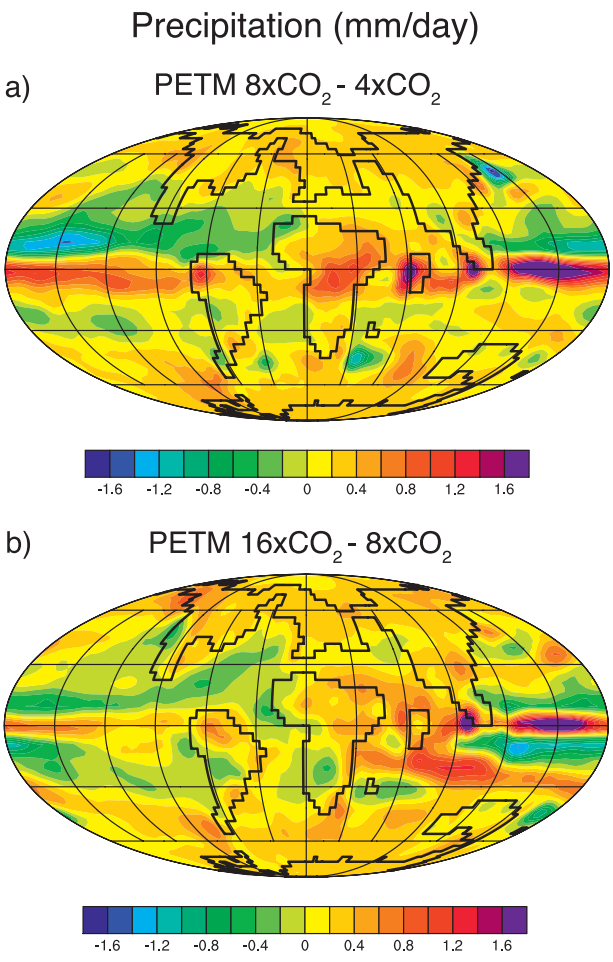

FIG. 7. Difference in 50-yr mean annual precipitation (mm day^{-1}) (a) between the 8×CO_2 and 4×CO_2 and (b) between the 16×CO_2 and 8×CO_2 PETM experiments.

precipitation values for increasing CO_2 forcing (Figs. 6 and 7).

Note that both precipitation and evaporation increase with an increase in the CO_2 radiative forcing (Fig. 5b). Higher precipitation and lower sea surface salinity values for high latitudes in the Northern Hemisphere are consistent with findings by Pagani et al. (2006a) and Sluijs et al. (2008a), who inferred increased weathering due to increased precipitation and low salinities from isotopic measurements as well as from dinoflagellate cyst assemblages in the Arctic. For the southern high latitudes, a simulated increase in precipitation is confirmed by clay-mineral indicators from the Antarctic continent, pointing toward humid conditions at the PETM (Robert and Kennett 1994). The enhanced precipitation at high latitudes is consistent with patterns simulated for future climate scenarios (e.g., Cubasch et al. 2001; Meehl et al. 2006; Mikolajewicz et al. 2007).

Seasonal variability in the PETM simulations is particularly high in the Indian Ocean in response to the paleogeography (Figs. 6b,c). Land–sea circulation is amplified by the PETM position of the Indian subcontinent between Africa and Asia. The proto-Himalaya (prior to the collision of India with Asia) is of low elevation so that the monsoonal circulation for the PETM is weaker than for the present day. Evidence from paleoproxies and modeling studies indicates that the variability and magnitude of the Indian monsoon intensified significantly with the uplift of the Himalayas, in particular during the

accelerated increase in height about 10 to 8 million years ago (e.g., Ruddiman and Kutzbach 1989; Kutzbach et al. 1993; An et al. 2001). Over southern subtropical East Africa, the seasonal precipitation in the $8\times CO_2$ experiment changes from <1 mm day^{-1} during the Southern Hemisphere winter [June–August (JJA)] up to 10 mm day^{-1} during the Southern Hemisphere summer [December–February (DJF)]. Figure 7 shows that with an increase in CO_2, precipitation in this area increases.

Analysis of precipitation patterns provides insights into potential terrestrial carbon sources and sinks. For example, an increase in methane fluxes from wetlands in England has been proposed for the PETM (Pancost et al. 2007), which is in agreement with simulated increasingly wet conditions at this location (from ~6 mm day^{-1} for $4\times CO_2$ to ~7 mm day^{-1} for $16\times CO_2$) with higher atmospheric CO_2 values (Figs. 6 and 7). Nutrient and carbon cycles of subtropical savannas in Africa, South America, and Southeast Asia are controlled by water availability (Wang et al. 2009). Thus, high precipitation during hot summer months and biomass burning through wildfires during dry winter months at the PETM could have provided a significant carbon release to the atmosphere (Fig. 7).

d. Surface winds

The simulated PETM atmospheric circulation is characterized by slightly weaker than present-day trade winds in response to a weaker than present-day Hadley cell (Figs. 8 and 9), consistent with the future-climate-change studies by Vecchi and Soden (2007). The trade winds from the $4\times CO_2$ run to the $16\times CO_2$ run decrease with an increase in greenhouse gases. The poleward shift in subpolar low pressure systems relative to the present-day run is also comparable with future climate scenarios (see Meehl et al. 2006). PETM and present-day Northern Hemisphere westerlies are comparable in strength, but Southern Hemisphere westerlies are significantly weaker than for present-day (Figs. 8 and 9), related to a lower meridional temperature gradient with an ice-free Antarctic region. Moreover, increased friction due to a narrow Drake Passage and a more southward position of Australia contribute to reduced PETM Southern Hemisphere westerlies. A significant seasonal variability (Fig. 9) in surface winds is simulated over the Atlantic and Indian Ocean. During Northern Hemisphere wintertime, a high pressure system over the Tethys and Southeast Asia contributes to strong northeast winds over Africa. In the Northern Hemisphere summer, with a northward shift of the ITCZ, warm moist air from the Tethys contributes to strong convective activity over North Africa. The high precipitation over Southeast Asia is related to moisture transport from the tropical Pacific and Indian Ocean.

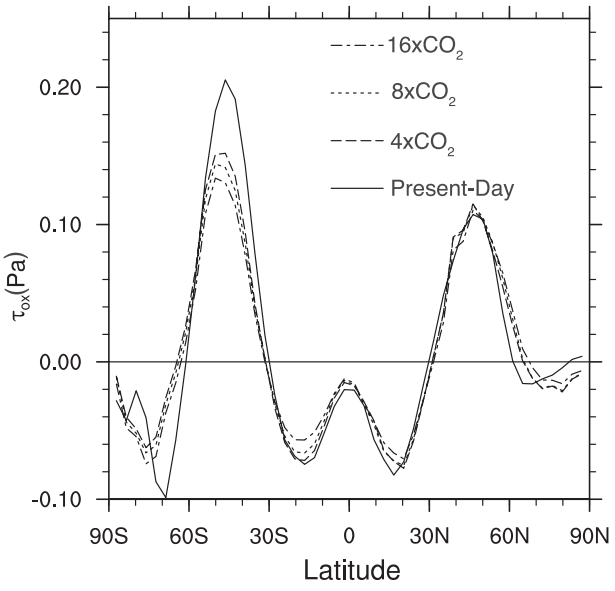

FIG. 8. Meridional profiles of the 50-yr mean zonal wind stress component over the ocean (Pa) for present day (solid), $4\times CO_2$ PETM (long dashed), $8\times CO_2$ PETM (short dashed), and $16\times CO_2$ PETM (dashed–dotted).

e. Changes in the jet stream

The tropospheric jet stream and the baroclinic wave activity are strongest during the PETM winter (Fig. 10) when the equator-to-pole gradient reaches its maximum. In comparison to the modern climate, the core of the subtropical jet stream shifts upward from ~12 km height by ~1 km because of an increase in temperature in the troposphere. In the Northern Hemisphere, the core of the jet stream shifts ~2° poleward, consistent with the slight poleward shift of the trade winds (Fig. 8). The poleward shift of the jet stream in a hothouse world is also in agreement with evidence of recent climate change, indicating that the tropics have already expanded poleward during 1979–2005 (Seidel et al. 2008).

Results from modeling studies (see section 3c) suggest that mountain uplift such as the formation of the Himalayas affects the jet stream and the global climate. The increase in the PETM subtropical jet stream intensity relative to the present day owing to an increase in the temperature gradient is partially compensated by lower altitudes of mountain chains over Asia and North America. In the Southern Hemisphere, the PETM jet stream north of Australia is stronger than at present because of the more polar location of the PETM Australian continent. With increasing atmospheric CO_2 concentrations, the jet stream over the PETM Atlantic intensifies slightly, related to a greater land-to-sea temperature gradient.

The stratospheric radiative cooling (section 3b) leads to significantly lower polar pressures and an enhanced

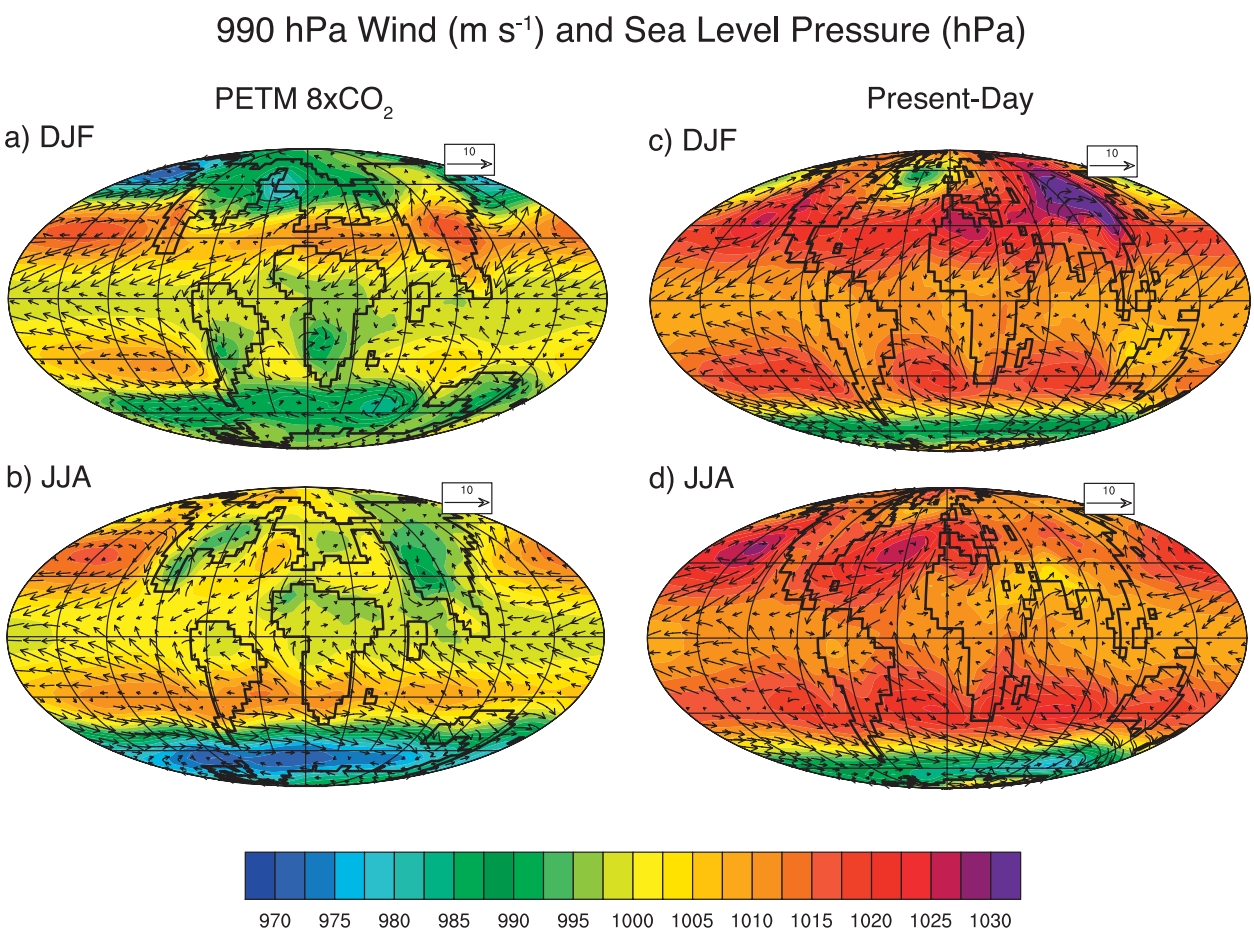

FIG. 9. The 990-hPa wind (vectors; m s^{-1}) and surface pressure (50-yr mean) (hPa) for the 8×CO_2 PETM experiment NH (a) winter (DJF) and (b) summer (JJA) and for the present-day experiment NH (c) winter (DJF) and (d) summer (JJA).

lower stratospheric jet stream that merges with the upper stratospheric jet stream.

4. Results from PETM simulations (ocean)

a. Sea surface temperature and surface currents

Simulated 8×CO_2 PETM global annual mean sea surface temperatures are 24.6°C (Table 1), with temperatures reaching as high as ~32°–35°C in tropical waters in the Indian Ocean, the Atlantic, and the western Pacific (Fig. 11a). Mean sea surface temperatures for the 4×CO_2 and 16×CO_2 PETM simulations are 1.9°C cooler and 2.5°C warmer, respectively, in response to the differences in CO_2 radiative forcing (Table 1). Simulated temperatures of the 8×CO_2 and the 16×CO_2 experiments fall within the range of tropical sea surface temperatures inferred from data in Tanzania (Table 2), using the TEX_{86} proxy and $\delta^{18}O$, which are 30°–34°C (Pearson et al. 2007). These temperature estimates might even be several degrees too low, according to a corrected calibration of the TEX_{86} proxy for temperatures above 30°C (Kim et al. 2008). In the tropical and subtropical North Pacific, PETM temperatures of 32°–35°C are indicated by planktonic foraminifera (ODP 865 and 1209, Fig. 1 and Table 2; Tripati and Elderfield 2005). Both of the 8×CO_2 and 16×CO_2 experiments match the estimates in the eastern part of the tropical Pacific (ODP 865, Fig. 1 and Table 2), which exhibits lower than zonal average surface temperatures due to strong Ekman-induced equatorial upwelling by trade winds (Figs. 9 and 12a). For the subtropical North Pacific location (ODP 1209, Fig. 1 and Table 2), results from the 8×CO_2 experiment lie ~5°–7°C below the data-inferred temperature. This bias is reduced by ~2.5°C in the 16×CO_2 experiment. The simulated east–west gradient in temperature is similar to the one in the present-day simulation, which agrees with observational data from Reynolds and Smith (1994) in the central Pacific (Yeager et al. 2006).

For the 8×CO_2 and 16×CO_2 simulations, temperatures >34°C are simulated in the western equatorial

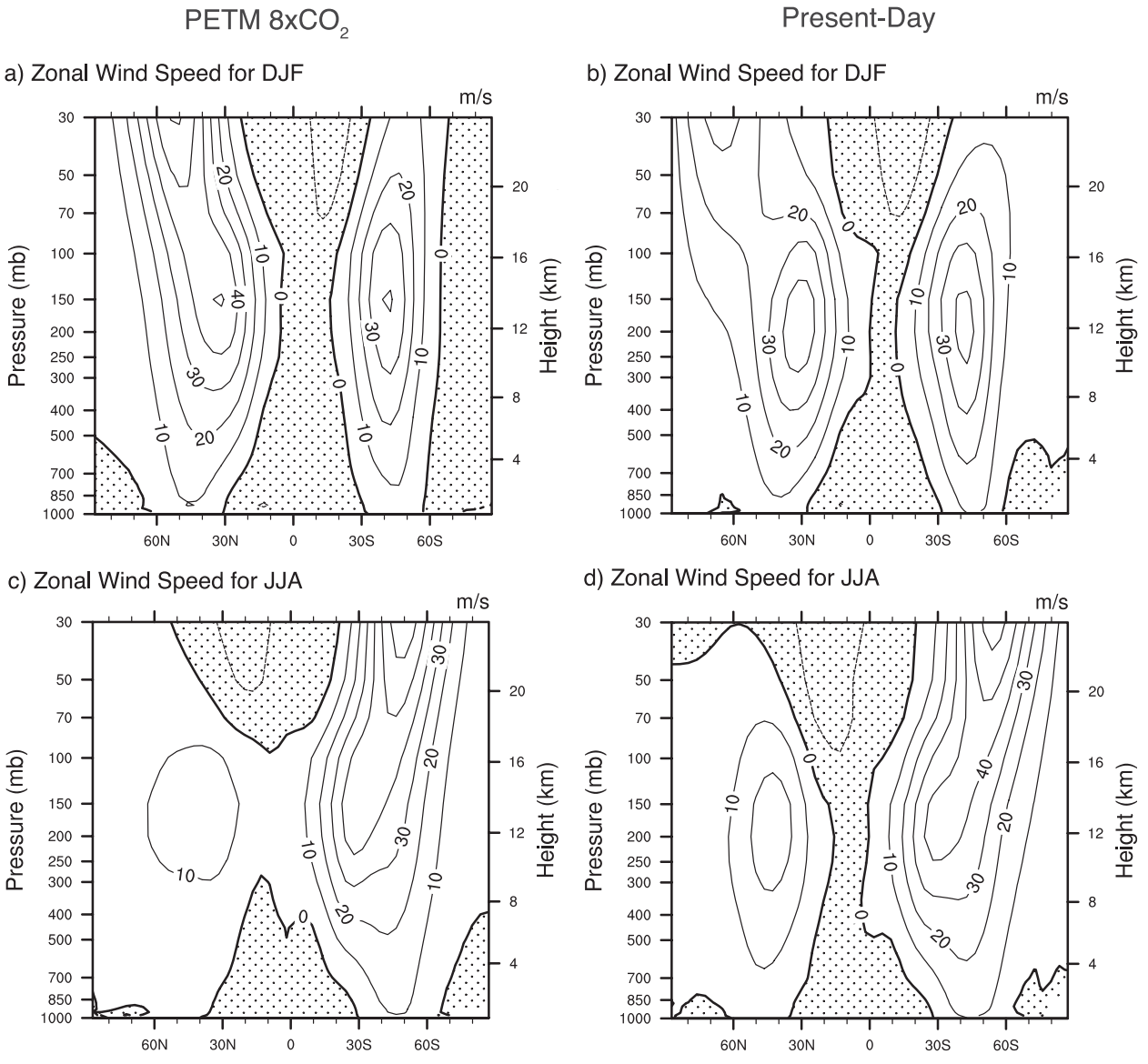

FIG. 10. Climatological 50-yr mean zonal wind speed: Winter (DJF) in the NH for (a) the PETM $8\times CO_2$ experiment and (b) the present day, and winter (JJA) in the SH for (c) the PETM $8\times CO_2$ experiment and (d) the present day. Contour interval is 10 m s^{-1}. The zero contour line is bold; positive contour values indicate westerlies and negative values indicate easterlies.

Pacific (similar to the present-day warm pool) and in the equatorial Indian Ocean. These areas are characterized by a highly stratified warm lens. Higher than average ocean temperatures in midlatitudes are associated with western boundary currents, up to 2°C warmer at 30°N in the western PETM North Pacific and at 30°S in Mozambique Strait. In the northwest Pacific, a change in wind stress and precipitation patterns (Fig. 7a) from $4\times CO_2$ to $8\times CO_2$ and the associated change in latent heat flux cause a shift in air and sea surface temperature (Figs. 4c and 11b), salinity (Fig. 13b), and the mixed layer depth (Fig. 16b), thereby reducing the formation of saline and warm intermediate-water masses in the PETM North Pacific (Fig. 18c). In the $16\times CO_2$ experiment, the midlatitude land–sea temperature gradient contrast near the east coast of Asia (Fig. 4b), and thus the direction and intensity of near-shore winds and the western boundary current, are comparable to the $8\times CO_2$ experiment (Fig. 11c). The simulated North Pacific circulation for $8\times CO_2$ consists of three gyres (Fig. 12). Counterclockwise surface winds in the PETM North Pacific low drive the subpolar gyre centered around 60°N (Figs. 9 and 12b). The pressure gradient between the PETM North Pacific low and the subtropical high is about 10 hPa higher than in the present-day simulation, resulting in an anticyclonic (clockwise) subtropical gyre

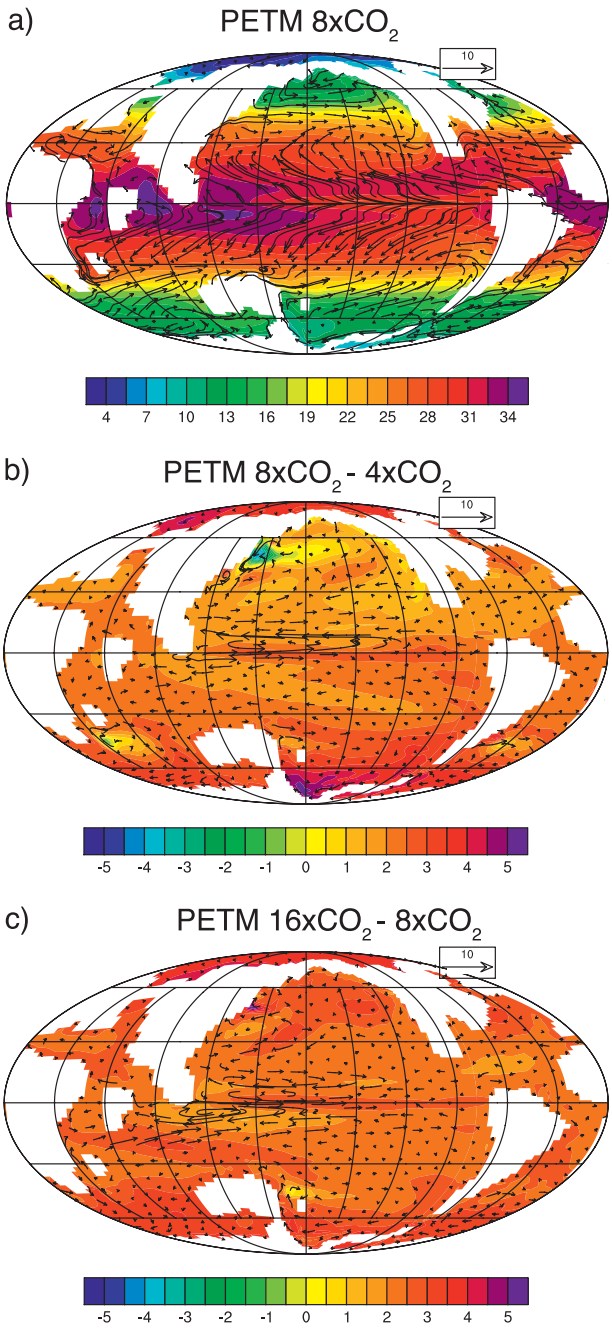

FIG. 11. Annual 50-yr mean sea surface temperature (°C) and horizontal velocities (vectors, cm s^{-1}) for (a) the 8×CO_2 PETM experiment and the difference (b) between the 8×CO_2 and 4×CO_2 and (c) between the 16×CO_2 and 8×CO_2 experiments.

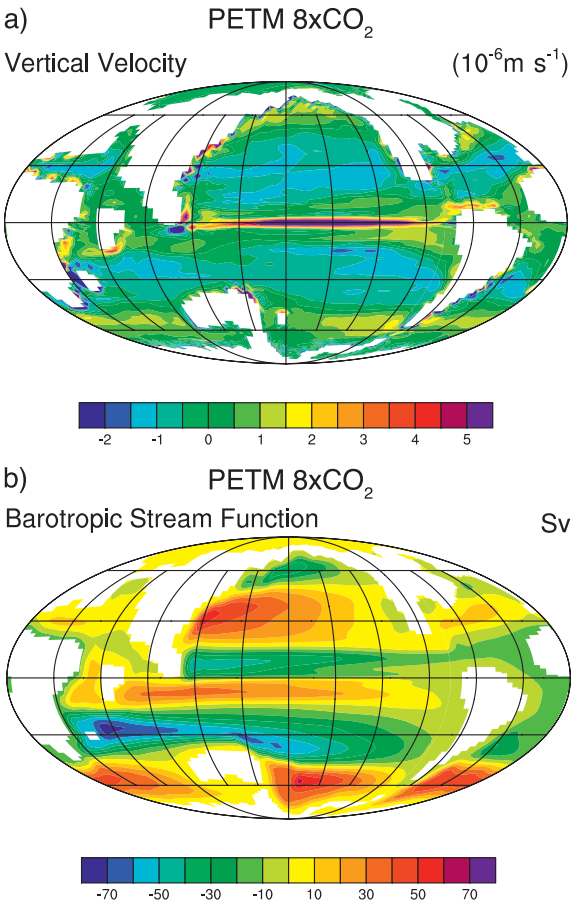

FIG. 12. (a) Annual vertical velocity (50-yr mean) (10^{-6} m s^{-1}) and (b) barotropic streamfunction (in Sv) for the 8×CO_2 PETM experiment.

~10 Sv (Sv ≡ 10^6 m^3 s^{-1}) stronger than in the present day, with a maximum transport of about 60 Sv.

Remarkable differences in the wind field between the PETM 8×CO_2 and the present-day simulation are displayed in Fig. 9. The narrow Atlantic and the Tethys favor a more southward location of the Atlantic high pressure system, shifting the simulated PETM North Atlantic Current ~10° more equatorward than at present. The narrow PETM northern North Atlantic is characterized by a cyclonic gyre (20 Sv, Fig. 12b) with a southward-directed cool polar current flowing to a latitude ~40°N along the North American east coast. Simulated summer temperatures in the 8×CO_2 scenario of ~29°C (~4°C above the annual mean) are underestimated by ~4°C compared to the TEX_{86} proxy-inferred coastal temperatures of ~33°C at Wilson Lake (Zachos et al. 2006; Fig. 1 and Table 2). Summer temperatures from the 16×CO_2 PETM scenario agree reasonably well with these paleotemperature estimates (Table 2).

Simulated high-latitude temperatures for the 8×CO_2 experiment near Antarctica are in the range from 11° to 15°C (Fig. 11a). Early Eocene shelf temperatures from Seymour Island off the Antarctic Peninsula, deduced from $\delta^{18}O$ values, lie between 6° and 18°C (Fig. 1 and Table 2; Ivany et al. 2008). Temperatures for the

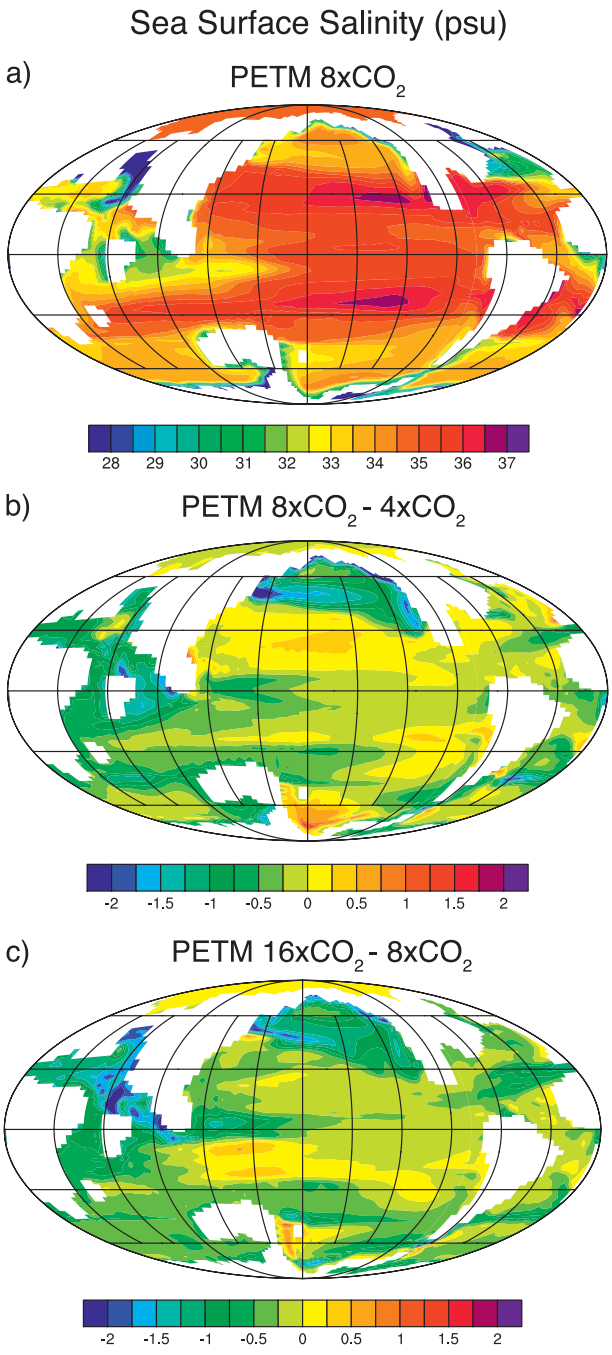

FIG. 13. Annual sea surface salinity (50-yr mean) (psu) for (a) the $8\times CO_2$ PETM experiment and the difference (b) between the $8\times CO_2$ and $4\times CO_2$ and (c) between the $16\times CO_2$ and $8\times CO_2$ PETM experiments.

$4\times CO_2$, $8\times CO_2$, and $16\times CO_2$ experiments are in agreement with this data range (Table 2). TEX_{86} reconstructions by Sluijs et al. (2006, 2008a) from the Lomonosov Ridge in the Arctic Ocean, as well as reconstructions by Weijers et al. (2007), point to temperatures peaking at 23°C at the PETM (Fig. 1), whereas annual mean temperatures at this location amount to 3°C in the $8\times CO_2$ and 7°C in the $16\times CO_2$ scenario (Table 2). If the data are skewed toward summer temperatures (Sluijs et al. 2006), the model − data error reduces to 12°C for the $16\times CO_2$ scenario. Uncertainties in the paleolocation may also contribute to the bias. For example, a locality closer to shore would reduce the model − data differences since the modeled temperature gradient in this area is very strong. The early Eocene TEX_{86}-inferred temperatures of 30°–37°C from the Waipara River in New Zealand, Fig. 1 (Hollis et al. 2009), might also be biased toward summer temperatures and/or represent a localized phenomenon. Our modeled mean annual temperature in this area is ~14°C for the $8\times CO_2$ simulation (Fig. 11a and Table 2), in agreement with the model results (by Huber) shown in Hollis et al. (2009). For the $16\times CO_2$ simulation, annual mean temperature is predicted to be ~3°C warmer than for the $8\times CO_2$ simulation. Summer temperature values for these two experiments amount to ~19°C and ~21°C, respectively.

Around Antarctica, sea surface temperature warms by 2°–4°C with a quadrupling of the atmospheric CO_2 concentration (from $4\times CO_2$ to $16\times CO_2$). This tendency of high-latitude warming is in general agreement with the high-latitude warming predicted for the future (Solomon et al. 2007). The barotropic streamfunction in the Southern Ocean is substantially weaker than in the present-day simulation due to a smaller than present-day temperature contrast (Fig. 3a) and wind stress (Fig. 8) related to the absence of an Antarctic ice sheet during the PETM as well as differences in the geography (a very narrow and shallow Drake Passage and more southward location of Australia). The narrow Drake Passage favors a northward-directed transport of polar water masses along the west coast of South America. The East Austral Current extension (Tilburg et al. 2001) is reversed in direction as part of a clockwise polar gyre east of proto-Australia during the PETM.

b. Sea ice

In the $4\times CO_2$ experiment, the annual average coverage of the ocean surface by sea ice is 3.6%, and sea ice coverage in the Arctic exists during the Northern Hemisphere winter only. In the $8\times CO_2$ simulation, sea ice is negligible (<0.05%). No sea ice at all appears in the $16\times CO_2$ scenario (Table 1) owing to an increase in high-latitude surface temperature with an increase in CO_2 radiative forcing (Figs. 4c,d). Sea ice has been inferred from ice-rafted debris for the middle Eocene, but not for the early Eocene (Moran et al. 2006; St. John 2008); particularly at the PETM, evidence from sediments suggests that the Arctic was ice free (Sluijs et al. 2006).

c. Salinity

Predictions of PETM surface salinity reflect the precipitation minus evaporation and freshwater entrainment from marginal seas and from rivers (Fig. 13). High salinities are simulated near subtropical high pressure systems in the Pacific and in high evaporation regions (Fig. 5b). An increase in sea surface temperature with an increase in CO_2 radiative forcing leads to elevated evaporative flux and a corresponding increase in the salinity (Figs. 13b,c). Low salinity surface conditions with $S < 30$ psu in the $8\times CO_2$ experiment (Fig. 13) are predicted for coastal areas south of the Turgay Strait in response to the high freshwater surplus arising from the Arctic marginal sea parameterization. Paleoproxies support a potentially low saline outflow from the relatively fresh PETM Arctic (section 3d). The surface salinity in the northeastern Tethys decreases in response to an increased high-latitude precipitation (Fig. 5a). The tendency of an increase in Arctic freshwater input with increasing atmospheric CO_2 leads to a corresponding decrease in the eastern Tethys salinity (Figs. 13b,c). Higher precipitation in the northern Indian Ocean region in a high-CO_2 world contributes to a significant freshening of the water masses, consistent with the increase in freshwater runoff into the Arctic inferred from a peak in *Apectodinium* (Crouch 2001; Pagani et al. 2006a) (section 3c).

d. Global overturning circulation and mixed layer depth

The running 5-yr mean smoothed sea surface temperature, deep-sea temperature, and global maximum meridional overturning circulation (MOC) for the PETM experiments are shown in Fig. 14. The sea surface temperature adjusts fairly quickly and equilibrates into the new state within ~200 years. The deep-sea adjustment in temperature is more sluggish with a small drift of $<0.01°C\ century^{-1}$ for the $8\times CO_2$ run and $\sim 0.1°C\ century^{-1}$ for the $4\times CO_2$ and $16\times CO_2$ simulations. The global deep-sea circulation in the PETM $8\times CO_2$ experiment is more sluggish than at present, Fig. 15 [for a detailed description of the present-day MOC see Yeager et al. (2006); Bryan et al. (2006)] owing to an enhanced vertical stratification related to warmer and fresher surface conditions at high latitudes (Figs. 15a,b). The very narrow and shallow Drake Passage and a more southward position of Australia during the PETM also contribute to a weaker circulation by obstructing the circumpolar flow of water masses. In the PETM Pacific, mixed layer depths >200 m (Fig. 16) are located in the Bering Sea and southeast of Australia. These areas of strong vertical mixing are sources of intermediate-water masses (Fig. 15c). In contrast to the present-day simulation, the PETM Atlantic (Fig. 15e) is stratified with no deep-water formation in the Northern Hemisphere, mostly because of the climatic influence of the surrounding continents (Figs. 11 and 13). Midocean ridges in the narrow juvenile Atlantic result in shallow water depth in the tropics, thus blocking the northward flow of deep-water masses below ~2000 m across the equator. The Southern Ocean overturning circulation cell is substantially reduced, related to the changes listed above and a lower than present-day meridional temperature gradient. High variability in the $4\times CO_2$ experiment (Fig. 14a) is linked to a deep maximum mixed layer depth by winter mixing in the North Pacific (Fig. 16b) and slightly declines over time in response to the adjustment of the deeper layers. With an increase of the atmospheric CO_2 from $8\times CO_2$ to $16\times CO_2$, high-latitude stratification increases significantly in response to a decrease in surface salinity and increase in surface temperature. The associated reduction in the mixed layer depth (Figs. 16a,c) south of New Zealand near Antarctica results in a reduction of the Southern Ocean overturning circulation cell by 3 Sv (Fig. 14d), thus enhancing climate sensitivity, whereas the already sluggish Northern Hemisphere deep water does not change significantly in strength (Figs. 14c and 16c).

Freshwater exchange through seaways other than Turgay Strait would also have influenced the climate. For example, freshwater input from the Arctic into the North Pacific would have produced an increase in the stratification and led to a weakening of the North Pacific Intermediate-Water masses by 2.5 Sv at 30°N, and a comparable increase in the Pacific deep-sea circulation. The heat transport in the North Pacific is reduced by ~0.2 PW when freshwater from the Arctic is added to the Pacific instead of the Indian Ocean (for details see Cope 2009).

e. Poleward ocean heat transport

The 20-yr-mean global northward heat transport is shown in Fig. 17, reflecting changes in the meridional sea surface temperature gradient and in the overturning circulation under the assumption of near-incompressibility of ocean water masses. It is remarkable that the range in the present-day observations exceeds the PETM − present-day differences. The difficulties associated with the estimate of the heat transport from observations include, for example, limitation of data to certain regions, a low amount of available data, and problems associated with quasi-stationary eddies. On the other hand, the estimates from model simulations depend on the model parameterizations (e.g., subgrid-scale eddies). As shown in Figs. 15 and 17, the heat transport in the PETM scenarios diminishes with a less vigorous meridional overturning

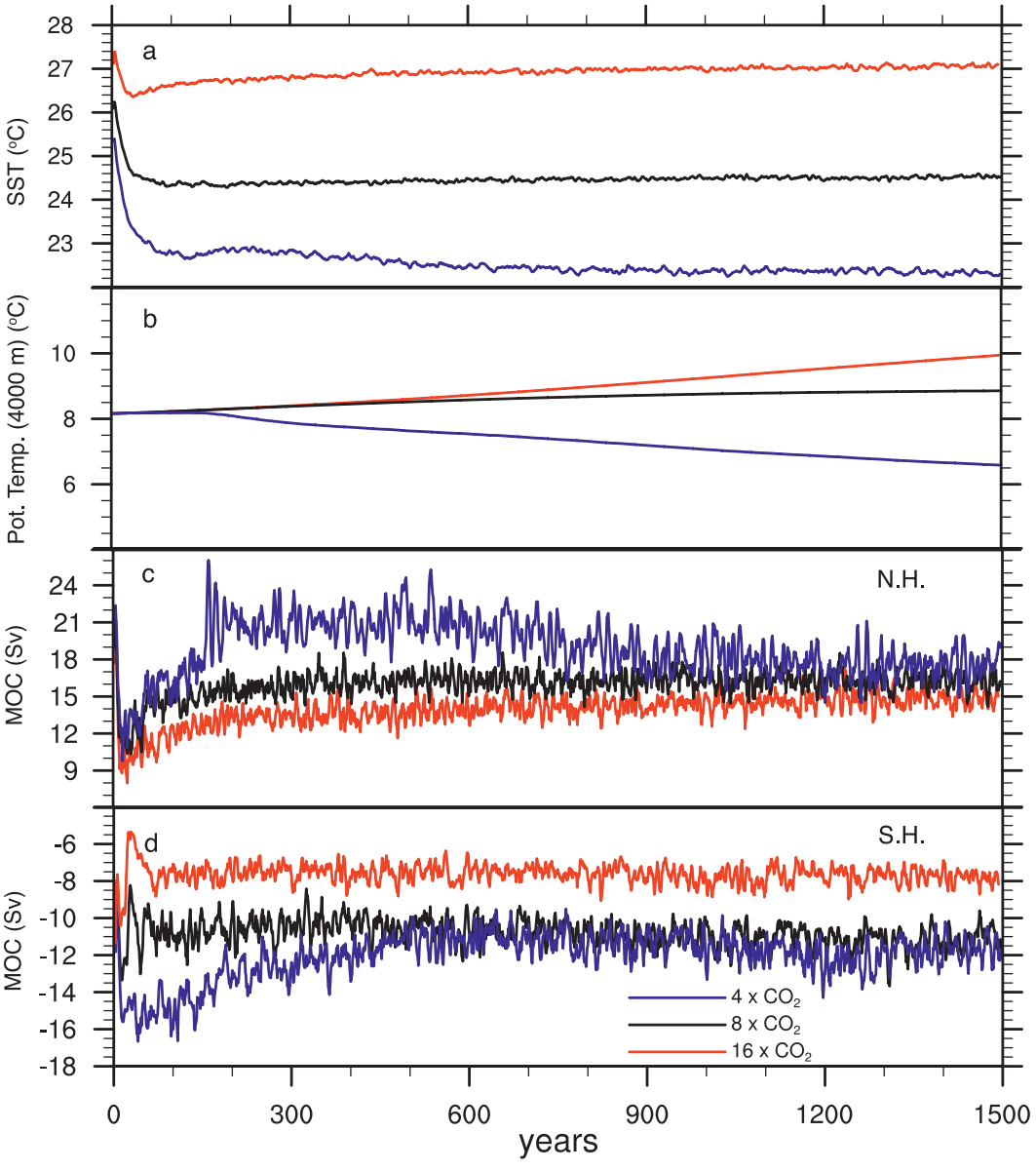

FIG. 14. (a) Time series of the global SST (°C), (b) global potential temperature at 4000-m depth (°C), and meridional overturning circulation (Sv) below 500 m in the (c) NH and (d) SH for 4×CO_2 PETM (blue), 8×CO_2 PETM (black), and 16×CO_2 PETM (red). Time series smoothed with 5-yr running mean.

circulation in response to the increased CO_2 radiative forcing. A significant reduction in the heat transport is particularly evident for the 16×CO_2 run, characterized by a weaker overturning circulation (relative to 8×CO_2, Fig. 14) and a reduced temperature gradient with an increased recirculation in the northern tropical gyre (Fig. 11c). For the 4×CO_2 and 8×CO_2 experiments, the heat transport in the Southern Hemisphere is stronger than at the present day, whereas in the extratropical Northern Hemisphere region it is diminished for the 8×CO_2 and 16×CO_2 simulations. A more symmetric appearance of the PETM poleward heat transport reflects the larger than present-day Pacific Ocean and smaller than present-day Atlantic Ocean.

f. Deep-sea temperatures

The Pacific vertical temperature distribution for the 8×CO_2 PETM simulation exhibits a strong vertical stratification in the subtropics and tropics. Equatorial water is separated from a well-mixed and homogeneous surface layer by a strong (and shallow relative to the

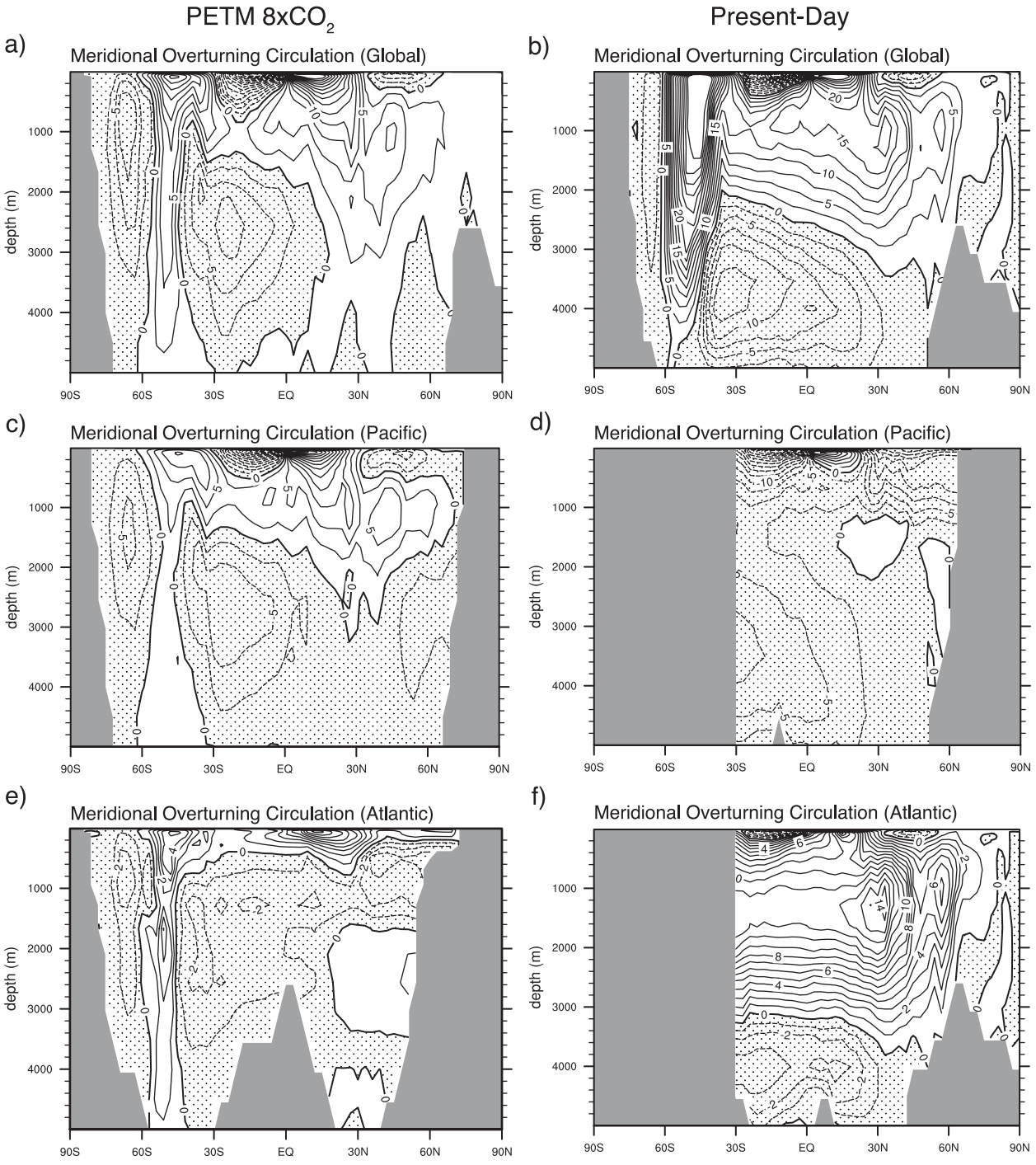

FIG. 15. Global Eulerian meridional overturning circulation (50-yr mean) (Sv) for (a) the 8×CO_2 PETM experiment and (b) the present-day experiment. (c)–(f) As in (a),(b), but (c),(d) for the Pacific and (e),(f) for the Atlantic.

subtropics) thermocline (Fig. 18a). Seasonal ventilation in northern and southern high latitudes (Figs. 15 and 16) is reflected in relatively cool temperatures of ~9°C in the deep sea. In contrast to the present day, the PETM Atlantic in the 8×CO_2 simulation is ventilated around 40°–50°S. Similar to the present-day Pacific, the North Atlantic is stratified and the strong vertical temperature gradient suppresses convective overturning (Fig. 18b). Differences between the 8×CO_2 and 4×CO_2 simulations in the Pacific exhibit increased stratification

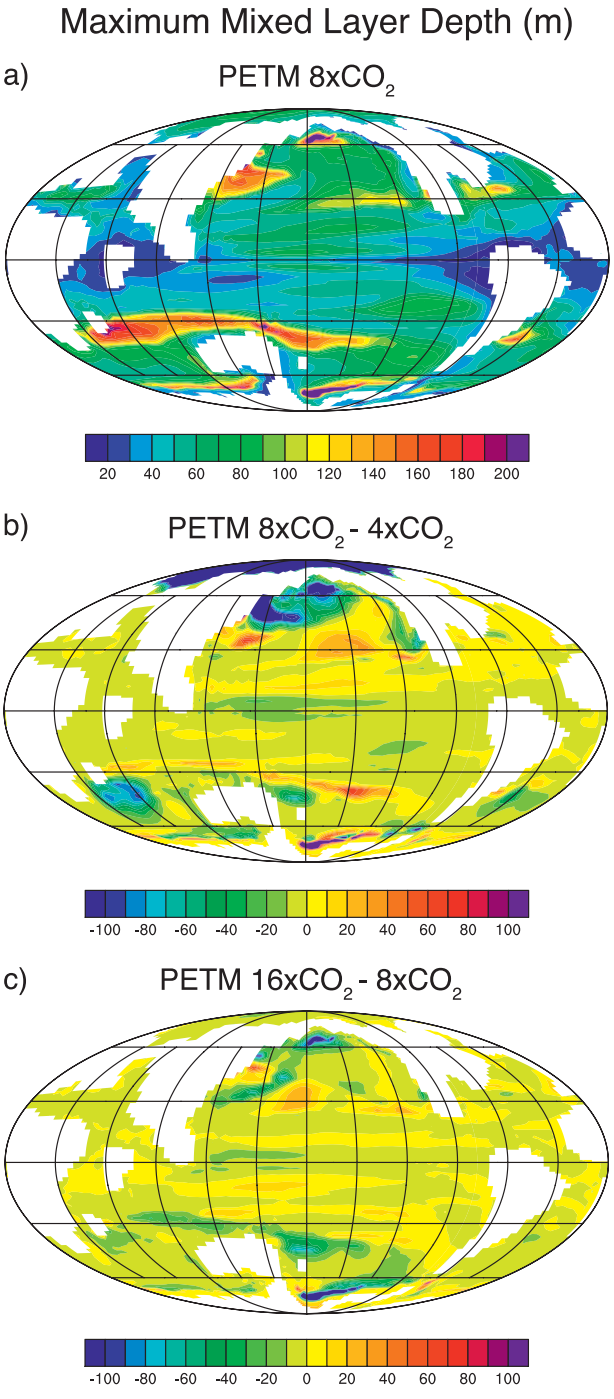

FIG. 16. Maximum mixed layer depth (m) for (a) the $8\times CO_2$ PETM experiment and the difference (b) between the $8\times CO_2$ and $4\times CO_2$ and (c) between the $16\times CO_2$ and the $8\times CO_2$ PETM experiments (c).

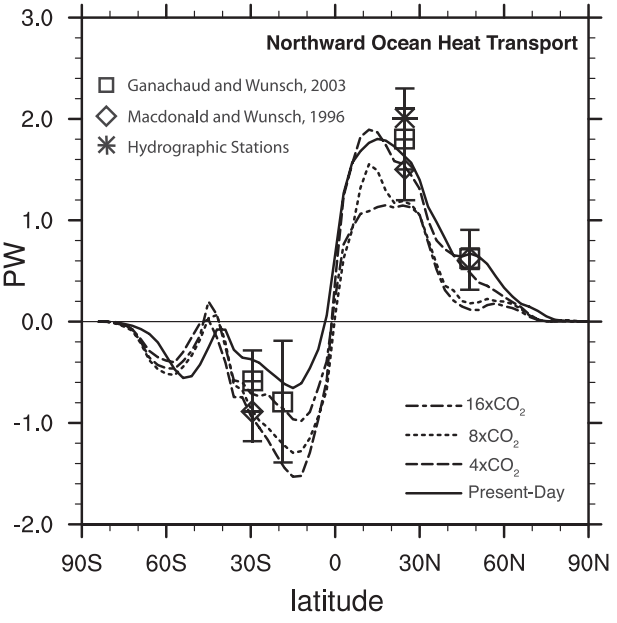

FIG. 17. Northward ocean heat transport (50-yr mean) (PW) for the present day (solid), $4\times CO_2$ PETM (long dashed), $8\times CO_2$ PETM (short dashed), and $16\times CO_2$ PETM (dashed–dotted). For comparison, results from inverse estimates (Macdonald and Wunsch 1996; Ganachaud and Wunsch 2003) and hydrographic observations (Bryden et al. 1991; Lavin et al. 1998) are shown.

and warm deep-sea temperature anomalies of ~2.5°C (Fig. 18c; section 4a).

A remarkable increase in stratification with an increase in intermediate-water mass temperatures of >3.75°C for the $8\times CO_2$ experiment relative to the $4\times CO_2$ experiment is simulated in the North Atlantic (Fig. 18d). The warm and saline water masses (~0.2 psu higher in salinity than in the $4\times CO_2$ experiment) originate from the Gulf of Mexico region and are mixed via the eastern North Atlantic into intermediate layers. Such a warming could correspond to a pre-PETM warming signal, as inferred from the Wilson Lake record (Sluijs et al. 2007a). A further high-latitude warming (for the $16\times CO_2$ experiment relative to the $8\times CO_2$ experiment) of >3.5°C is simulated for intermediate-water masses poleward of 30°N and >30°S in the Pacific owing to an increase in stratification by an increase in buoyancy fluxes (sections 4a and 4b).

Deep-sea model − data differences are given in Table 3. The closest match to the observations is simulated with $16\times CO_2$ PETM. A general bias of ~2°C is simulated for the tropical and subtropical sites, whereas significant discrepancies are evident for the Southern Ocean, in particular for the Waipara River location (New Zealand).

5. Comparison with previous model studies

A direct comparison with previous modeling studies is difficult because of the differences in initial conditions, model components, and boundary conditions. Details of model improvements of CCSM3 as applied in this study

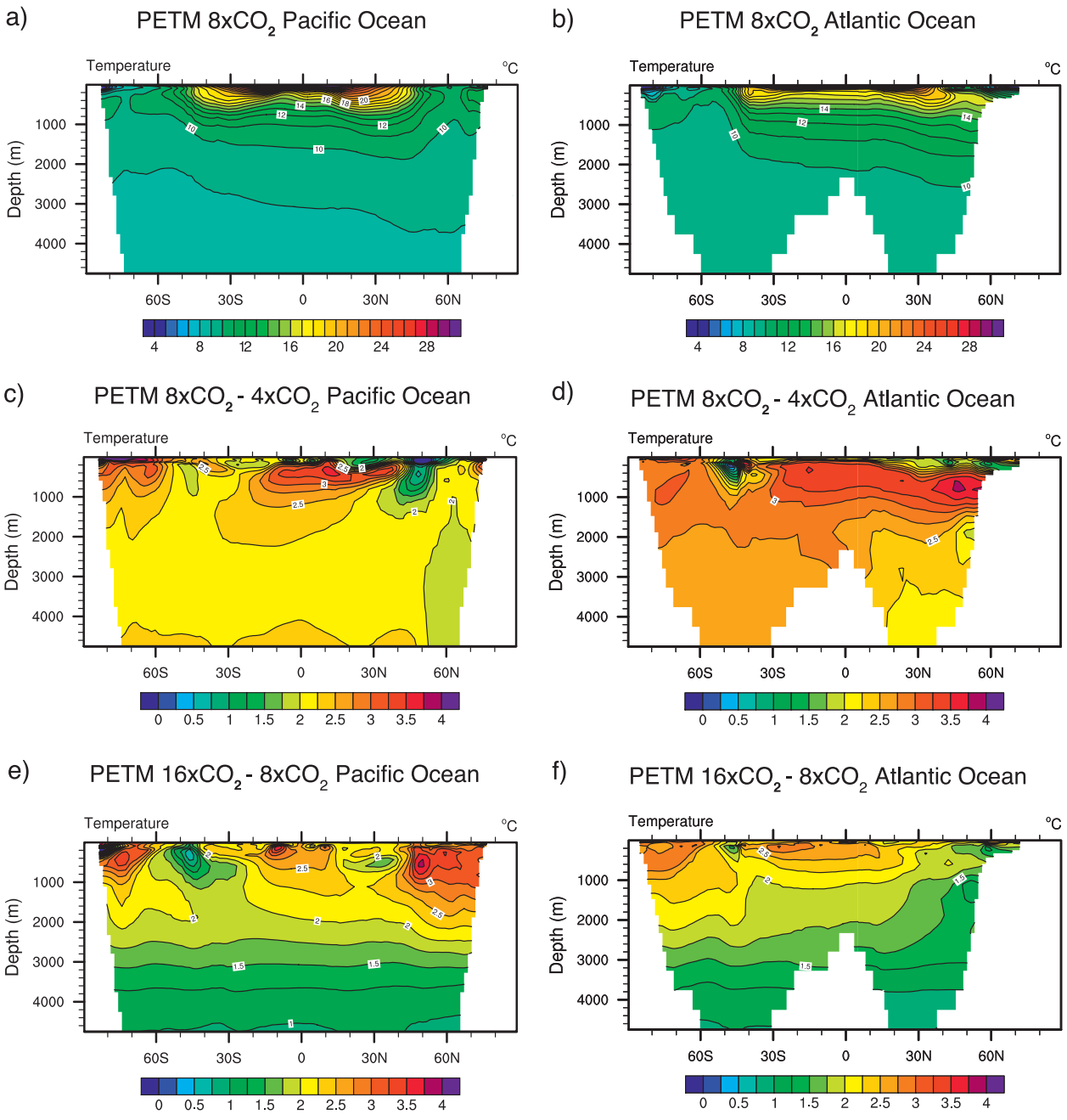

FIG. 18. Vertical sections of the potential temperature (50-yr mean): $8\times CO_2$ PETM for (a) the Pacific and (b) the Atlantic Ocean and differences between the $8\times CO_2$ and $4\times CO_2$ PETM experiments for the (c) Pacific and (d) Atlantic Ocean and between the $16\times CO_2$ and $8\times CO_2$ PETM experiments for the (e) Pacific and (f) Atlantic Ocean.

are given in Kiehl and Gent (2004) and Collins et al. (2006a).

Many of the previous PETM climate simulations have used an atmospheric general circulation model (AGCM) with a mixed layer parameterized in the form of a slab ocean (e.g., Sloan and Rea 1996; Huber and Sloan 2001; Shellito et al. 2003). As described in Shellito et al. (2003), the $HiCO_2$ case (with an atmospheric pCO_2 of 2000 ppmv, corresponding to 7.14 × preindustrial atmospheric pCO_2) simulates coastal temperatures that were above freezing. The freezing temperature in the Shellito et al. (2003) $HiCO_2$ case occurs at ~80°N, whereas our $8\times CO_2$ simulation predicts ice-free poles with annual average temperatures of 2°–4°C. These model − model

TABLE 3. Intermediate depth and deep-sea temperatures from data and modeled temperatures (annual average) for some of the locations shown in Fig. 1 (Zachos et al. 2004; Bralower et al. 2006; and references from Fig. 1). Paleolocations have been calculated using the PointTracker software by C. Scotese.

Name	Paleolocation	Paleodepth (m)	Data (°C)	Age	4×CO_2 (°C)	8×CO_2 (°C)	16×CO_2 (°C)
DSDP 277	~60.6°S, 170.7°W	Seafloor	~15	~51 Ma	6.4	8.7	9.7
Waipara River	~52.1°S, 160.8°W	Intermediate	19–24	~51 Ma	6.9–7.5	9.1–9.5	11.2–11.5
ODP 690	~65.7°S, 7.2°W	~2100	14–18	PETM	6.6	9.3	11.3
DSDP 74	~34.8°S, 10.5°W	~3100–3400	14–15	PETM	6.6	9.2	10.6
ODP 865	~8.3°N, 151.4°W	~1300	13–17	PETM	8.0	10.4	12.7
ODP 1209	~23.6°N, 171.1°W	~2400	13–21	PETM	7.3	9.4	11.2

differences are potentially related to the underestimated prescribed Southern Hemisphere ocean heat transport in the uncoupled model.

A higher response of the ocean heat transport to temperature gradients has been simulated with the GFDL Modular Ocean Model version 1.0 forced one-way with an output from an AGCM (e.g., Bice et al. 2000). The approach yielded a far more vigorous ocean heat transport than predicted by the AGCM alone and by the CCSM3 (this study). The different response appears to be related to the one-way forcing of the OGCM, missing interactive feedbacks between the atmosphere and the ocean.

A previous coupled CCSM1 2×CO_2 Eocene run, performed by Huber and Sloan (2001), predicted warmer than present-day temperatures in the tropics (3°C) and high latitudes (5°C), but the slightly lower than present-day pole-to-equator temperature gradient was still significantly higher than the one reconstructed from the temperature proxies.

6. Summary and conclusions

In this paper, the sensitivity of the simulated PETM climate to greenhouse gas forcing has been investigated with the comprehensive climate model CCSM3 with the goals of determining the effect of a change in greenhouse forcing on the formation of intermediate-water masses and whether CCSM3 produces a better match with proxies than previous modeling studies. In summary, the increase in greenhouse gas concentrations leads to a significant increase in stratification of the deep sea in the world's oceans and a shift in the intermediate-water masses. An externally triggered atmospheric CO_2 concentration increase from 4 × to 8 × the preindustrial value (e.g., volcanism-induced, Svensen et al. 2004; Storey et al. 2007; Sluijs et al. 2007a) might have favored warmer and more saline subtropical water masses originating near the Gulf of Mexico, one of the large present-day reservoirs of methane hydrates. The stability of gas hydrates predominantly depends on pressure, temperature, salinity, and gas composition. Suitable conditions for methane hydrates, depending on the water temperature, occur at water depths of ~250–3000 m along the slope and continental rise (see Fig. 1 in Dickens et al. 1995). The simulated temperature increase of ~4°C (from ~11° to ~15°C) in the intermediate-water masses in the North Atlantic from the 4×CO_2 to the 8×CO_2 PETM simulations would have lowered the depth of methane hydrate stability from ~900 to ~1400 m and hence could have led to a massive methane hydrate release into the atmosphere–ocean system.

The climatic conditions generated before the PETM might also have led to an enhanced greenhouse gas input from land reservoirs. Recent carbon isotope excursion data from Tanzania imply the release of larger quantities of ^{13}C-depleted carbon than inferred from many previous marine sedimentary records, but the exact amount of carbon addition, as well as its sources, remains controversial (see Handley et al. 2008, and discussion herein).

The model improvements in CCSM3 have reduced the bias between the predicted and reconstructed temperatures for the PETM. The most extreme simulation, with 16 × the preindustrial atmospheric CO_2 concentration, yields a closer match to the reconstructed temperature and precipitation proxies, with average tropical temperatures of 34°C and average temperatures above freezing (6°–8°C) at the poles, than the 8×CO_2 and 4×CO_2 simulations. However, a relatively high bias between simulated and data-inferred temperatures remains for some high-latitude locations and all deep-sea locations (with a bias between data and the 16×CO_2 experiment ranging from 0.3°C in the tropics to 5°C in the high latitudes). Possible reasons for model − data biases at high latitudes during hothouse climates and the resulting deep-sea temperature discrepancies have been discussed in several papers (see Washington and Parkinson 2005 and references therein). Many important processes are still missing in this climate simulation, for example the consideration of feedbacks with the atmospheric chemistry [e.g., volatile organic carbons, dimethylsulfide, and methane (Beerling et al. 2007; Lamarque et al. 2007) or methane oxidation in the atmosphere and its effect on stratospheric water vapor

(Schmidt and Schindell 2003)] or interactive vegetation. Changes in high-latitude tropospheric cloud condensation nuclei could also contribute to significant warming in the high latitudes, as demonstrated by Kump and Pollard (2008) for the Cretaceous. Other mechanisms commonly invoked as possible contributors to increased warming at high latitudes are polar stratospheric clouds (Sloan and Pollard 1998; Kirk-Davidoff et al. 2002) or intensified tropical cyclone activity (Korty et al. 2008). Using more extreme orbital settings in the simulations, Fig. 2 (see also Sloan and Huber 2001) might also increase summer surface temperatures in the high latitudes. Changes in orbital parameters are thought to act as one of the possible triggering mechanisms for hydrothermal events such as the ELMO event two million years after the PETM but with similar geochemical characteristics (Lourens et al. 2005).

It would be desirable to include the aforementioned improved model parameterizations into future higher-resolved simulations in order to simulate the past climate and climate variability in greater detail.

Acknowledgments. The graphics have been produced by Chandrika Nagaraj and Vinit Asher at UTA. We thank Jeff Kiehl, Stephen Yeager, and Keith Lindsay at NCAR for stimulating discussions and technical support. The comments by two anonymous reviewers greatly improved the quality of the manuscript. We thank Chris Scotese for providing an updated paleogeographic map for 55 Ma as well as the PointTracker Software. All model simulations were done on NCAR computers, supported by NSF. The work is supported by NSF Grant EAR-0628336.

REFERENCES

An, Z., J. E. Kutzbach, W. L. Prell, and S. C. Porter, 2001: Evolution of Asian monsoons and phased uplift of the Himalaya–Tibetan plateau since Late Miocene times. *Nature,* **411,** 62–66.

Barron, E. J., W. W. Hay, and S. Thompson, 1989: The hydrologic cycle: A major variable during Earth history. *Global Planet. Change.,* **1,** 157–174.

Beerling, D. J., C. N. Hewitt, J. A. Pyle, and J. A. Raven, 2007: Critical issues in trace gas biogeochemistry and global change. *Philos. Trans. Roy. Soc. London,* **365A,** 1629–1642.

Bice, K. L., and J. Marotzke, 2002: Could changing ocean circulation have destabilized methane hydrate at the Paleocene/Eocene boundary? *Paleoceanography,* **17,** 1018, doi:10.1029/2001PA000678.

——, C. R. Scotese, D. Seidov, and E. J. Barron, 2000: Quantifying the role of geographic change in Cenozoic ocean heat transport using uncoupled atmosphere and ocean models. *Palaeogeogr. Palaeoclimatol. Palaeoecol.,* **161,** 295–310.

Bowen, G. J., and B. B. Bowen, 2008: Mechanisms of PETM global change constrained by a new record from central Utah. *Geology,* **36,** 379–382.

——, and ——, 2009: Mechanisms of PETM global change constrained by a new record from central Utah: Reply. *Geology,* **37,** e185.

——, D. J. Beerling, P. L. Koch, J. C. Zachos, and T. Quattlebaum, 2004: A humid climate state during the Paleocene/Eocene thermal maximum. *Nature,* **432,** 495–499.

Bralower, T. J., D. J. Thomas, J. C. Zachos, M. M. Hirschmann, U. Röhl, H. Sigurdsson, E. Thomas, and D. L. Whitney, 1997: High-resolution records of the late Paleocene thermal maximum and circum-Caribbean volcanism: Is there a causal link? *Geology,* **25,** 963–967.

——, I. Premoli Silva, and M. J. Malone, 2006: 1. Leg 198 Synthesis: A remarkable 120-m.y. record of climate and oceanography from Shatsky Rise, Northwest Pacific Ocean. *Proc. Ocean Drilling Program, Sci. Results,* **198,** 1–47. [Available online at http://www-odp.tamu.edu/publications/198_SR/synth/synth.htm.]

Briegleb, B. P., C. M. Bitz, E. C. Hunke, W. H. Lipscomb, M. M. Holland, J. L. Schramm, and R. E. Moritz, 2004: Scientific description of the sea ice component in the Community Climate Model, version 3. NCAR Tech Note NCAR/TN-463+STR, 70 pp.

Brinkhuis, H., and Coauthors, 2006: Episodic fresh surface waters in the Eocene Arctic Ocean. *Nature,* **441,** 606–609.

Bryan, F., G. Danabasoglu, N. Nakashiki, Y. Yoshida, D.-H. Kim, J. Tsutsui, and S. Doney, 2006: Response of North Atlantic thermohaline circulation and ventilation to increasing carbon dioxide in CCSM3. *J. Climate,* **19,** 2382–2397.

Bryden, H., D. H. Roemmich, and J. A. Church, 1991: Ocean heat transport across 24°N in the Pacific. *Deep-Sea Res.,* **38,** 297–324.

Caldeira, K., and J. F. Kasting, 1992: The life span of the biosphere revisited. *Nature,* **360,** 721–723.

Collins, W. D., and Coauthors, 2006a: The Community Climate System Model version 3 (CCSM3). *J. Climate,* **19,** 2122–2143.

——, and Coauthors, 2006b: The formulation and atmospheric simulation of the Community Atmosphere Model version 3 (CAM3). *J. Climate,* **19,** 2144–2161.

Cope, J., 2009: On the sensitivity of the Eocene ocean circulation to arctic freshwater pulses. M.S. thesis, University of Texas at Arlington, 99 pp.

Crouch, E., 2001: Environmental change at the time of the Paleocene–Eocene biotic turnover. Ph.D. dissertation, Utrecht University, 216 pp.

Cubasch, U., and Coauthors, 2001: Projections of future climate change. *Climate Change 2001: The Scientific Basis,* J. T. Houghton et al., Eds., Cambridge University Press, 525–582.

Dickens, G. R., J. R. O'Neil, D. K. Rea, and R. M. Owen, 1995: Dissociation of oceanic methane hydrate as a cause of the carbon isotope excursion at the end of the Paleocene. *Paleoceanography,* **10,** 965–971.

——, M. M. Castillo, and J. C. G. Walker, 1997: A blast of gas in the latest Paleocene: Simulating first-order effects of massive dissociation of methane hydrate. *Geology,* **25,** 259–262.

Fricke, H. C., and S. L. Wing, 2004: Oxygen isotope and paleobotanical estimates of temperature and δ^{18}O-latitude gradients over North America during the early Eocene. *Amer. J. Sci.,* **304,** 612–635.

Ganachaud, A., and C. Wunsch, 2003: Large-scale ocean heat and freshwater transports during the World Ocean Circulation Experiment. *J. Climate,* **16,** 696–705.

Gent, P. R., F. O. Bryan, G. Danabasoglu, K. Lindsay, D. Tsumune, M. W. Hecht, and S. C. Doney, 2006: Ocean chlorofluorocarbon and heat uptake during the twentieth century in the CCSM3. *J. Climate,* **19,** 2366–2381.

Handley, L., P. N. Pearson, I. K. McMillan, and R. D. Pancost, 2008: Large terrestrial and marine carbon and hydrogen isotope excursions in a new Paleocene/Eocene boundary section from Tanzania. *Earth Planet. Sci. Lett.,* **275,** 17–25.

Head, J. J., J. I. Bloch, A. K. Hastings, J. R. Bourque, E. A. Cadena, F. A. Herrera, P. D. Polly, and C. A. Jaramillo, 2009: Giant boid snake from the Palaeocene neotropics reveals hotter past equatorial temperatures. *Nature,* **457,** 715–717.

Higgins, J. A., and D. P. Schrag, 2006: Beyond methane: Towards a theory for Paleocene–Eocene Thermal Maximum. *Earth Planet. Sci. Lett.,* **245,** 523–537.

Holland, M. M., C. M. Bitz, E. C. Hunke, W. H. Lipscomb, and J. L. Schramm, 2006: Influence of the sea ice thickness distribution on polar climate in CCSM3. *J. Climate,* **19,** 2398–2414.

Hollis, C. J., and Coauthors, 2009: Tropical sea temperatures in the high-latitude South Pacific during the Eocene. *Geology,* **37,** 99–102.

Houghton, J. T., G. J. Jenkins, and J. J. Ephraums, Eds., 1990: *Climate Change: The IPCC Scientific Assessment*. Cambridge University Press, 365 pp.

Houghton, J. T., Y. Ding, D. J. Griggs, M. Noguer, P. J. van der Linden, X. Dai, K. Maskell, and C. A. Johnson, Eds., 2001: *Climate Change 2001: The Scientific Basis*. Cambridge University Press, 881 pp.

Huber, M., 2009: Snakes tell a torrid tale. *Nature,* **457,** 669–671.

——, and L. C. Sloan, 1999: Warm climate transitions: A general circulation modeling study of the late Paleocene Thermal Maximum (~56 Ma). *J. Geophys. Res.,* **104,** 16 633–16 655.

——, and ——, 2001: Heat transport, deep waters, and thermal gradients: Coupled simulation of an Eocene greenhouse climate. *Geophys. Res. Lett.,* **28,** 3481–3484.

——, and R. Caballero, 2003: Eocene El Niño: Evidence for robust tropical dynamics in the ''hothouse.'' *Science,* **299,** 877–881.

Iakokleva, A. I., H. Brinkhuis, and C. Cavagnetto, 2001: Late Paleocene–early Eocene dinoflagellae cysts from the Turgay Strait, Kazakhstan; correlations across ancient seaways. *Palaeogeogr. Palaeoclimatol. Palaeoecol.,* **172,** 243–268.

Ivany, L. C., K. C. Lohmann, F. Hasiuk, D. B. Blake, A. Glass, R. B. Aronson, and R. M. Moody, 2008: Eocene climate record of a high southern latitude continental shelf: Seymour Island, Antarctica. *Geol. Soc. Amer. Bull.,* **120,** 659–678.

Kelly, D. C., T. J. Bralower, and J. C. Zachos, 1998: Evolutionary consequences of the latest Paleocene thermal maximum for tropical planktonic foraminifera. *Palaeogeogr. Palaeoclimatol. Palaeoecol.,* **141,** 139–161.

Kennett, J. P., and L. D. Stott, 1991: Abrupt deep-sea warming, palaeoceanographic changes and benthic extinctions at the end of the Palaeocene. *Nature,* **353,** 225–229.

Kiehl, J., and P. Gent, 2004: The Community Climate System Model, version 2. *J. Climate,* **17,** 3666–3682.

Kim, J.-H., S. Schouten, E. C. Hopmans, B. Donner, and J. S. Sinninghe Damsté, 2008: Global sediment core-top calibration of the TEX_{86} paleothermometer in the ocean. *Geochim. Cosmochim. Acta,* **72,** 1154–1173.

Kirk-Davidoff, B. D., D. P. Schrag, and J. G. Anderson, 2002: On the feedback of stratospheric clouds on polar climate. *Geophys. Res. Lett.,* **29,** 1556, doi:10.1029/2002GL014659.

Koch, P. L., J. C. Zachos, and P. D. Gingerich, 1992: Correlation between isotope records in marine and continental carbon reservoirs near the Palaeocene/Eocene boundary. *Nature,* **358,** 319–322.

Korty, R. L., K. A. Emanuel, and J. R. Scott, 2008: Tropical cyclone–induced upper ocean mixing and climate: Application to equable climates. *J. Climate,* **21,** 638–654.

Kump, L. R., and D. Pollard, 2008: Amplification of Cretaceous warmth by biological cloud feedbacks. *Science,* **320,** 195.

Kutzbach, J. E., W. Prell, and W. F. Ruddiman, 1993: Sensitivity of Eurasian climate to surface uplift of the Tibetan Plateau. *J. Geol.,* **101,** 177–190.

Lamarque, J.-F., J. T. Kiehl, and J. J. Orlando, 2007: The role of hydrogen sulfide in a Permian–Triassic Boundary ozone collapse. *Geophys. Res. Lett.,* **34,** L02801, doi:10.1029/2006GL028384.

Lavin, A., L. Bryden, and G. Parilla, 1998: Meridional transport and heat flux variations in the subtropical North Atlantic. *Global Atmos. Ocean Syst.,* **6,** 269–293.

Lourens, L. J., A. Sluijs, D. Kroon, J. C. Zachos, E. Thomas, U. Röhl, J. Bowles, and I. Raffi, 2005: Astronomical pacing of late Paleocene to early Eocene global warming events. *Nature,* **435,** 1083–1087.

Lu, G., G. Keller, and A. Pardo, 1998: Stability and change in Tethyan planktic foraminifera across the Paleocene–Eocene transition. *Mar. Micropaleontol.,* **35,** 203–233.

Lyle, M., J. Barron, T. J. Bralower, M. Huber, A. Olivarez Lyle, A. C. Ravelo, D. K. Rea, and P. A. Wilson, 2008: Pacific Ocean and Cenozoic evolution of climate. *Rev. Geophys.,* **46,** RG2002, doi:10.1029/2005RG000190.

Macdonald, A. M., and C. Wunsch, 1996: An estimate of global ocean circulation and heat fluxes. *Nature,* **382,** 436–439.

Maclennan, J., and S. M. Jones, 2006: Regional uplift, gas hydrate dissociation and the origins of the Paleocene–Eocene Thermal Maximum. *Earth Planet. Sci. Lett.,* **245,** 65–80.

Manabe, S., R. J. Stouffer, M. J. Spelman, and K. Bryan, 1991: Transient responses of a coupled ocean–atmosphere model to gradual changes of atmospheric CO_2. Part I: Annual mean response. *J. Climate,* **4,** 785–818.

Marincovich, L., Jr., and A. Y. Gladenkov, 1999: Evidence for an early opening of the Bering Strait. *Nature,* **397,** 149–151.

Markwick, P. J., 1997: Fossil crocodilians as indicators of Late Cretaceous and Cenozoic climates: Implications for using palaeontological data in reconstructing palaeoclimate. *Palaeogeogr. Palaeoclimatol. Palaeoecol.,* **137,** 205–271.

Meehl, G. A., and Coauthors, 2006: Climate change projections for the twenty-first century and climate change commitment in the CCSM3. *J. Climate,* **19,** 2597–2616.

Mikolajewicz, U., M. Gröger, E. Maier-Reimer, G. Schurgers, M. Vizcaíno, and A. Winguth, 2007: Long-term effects of anthropogenic CO_2 emissions simulated with a complex earth system model. *Climate Dyn.,* **28,** 599–633.

Moran, K., and Coauthors, 2006: The Cenozoic palaeoenvironment of the Arctic Ocean. *Nature,* **441,** 601–605.

Nunes, F., and R. D. Norris, 2006: Abrupt reversal in ocean overturning during the Palaeocene/Eocene warm period. *Nature,* **439,** 60–63.

Oglesby, R. J., 1989: A GCM study of Antarctic glaciation. *Climate Dyn.,* **3,** 135–156.

Oleson, K. W., and Coauthors, 2004: Technical description of the Community Land Model (CLM). NCAR Tech. Note TN-461+STR, 174 pp.

Otto-Bliesner, B. L., R. Tomas, E. C. Brady, C. Ammann, Z. Kothavala, and G. Clauzet, 2006: Climate sensitivity of moderate- and low-resolution versions of CCSM3 to preindustrial forcings. *J. Climate,* **19,** 2567–2583.

Pagani, M., and Coauthors, 2006a: Arctic hydrology during global warming at the Paleocene/Eocene thermal maximum. *Nature,* **442,** 671–675; Corrigendum, **443,** 598.

——, K. Caldeire, D. Archer, and J. C. Zachos, 2006b: An ancient carbon mystery. *Science,* **314,** 1556–1557.

Panchuk, K., A. Ridgwell, and L. R. Kump, 2008: Sedimentary response to Paleocene–Eocene Thermal Maximum carbon release: A model–data comparison. *Geology,* **36,** 315–318.

Pancost, R. D., D. S. Steart, L. Handley, M. E. Collinson, J. J. Hooker, A. C. Scott, N. V. Grassineau, and I. I. Glasspool, 2007: Increased terrestrial methane cycling at the Palaeocene–Eocene thermal maximum. *Nature,* **449,** 332–335.

Pearson, P. N., and M. R. Palmer, 2000: Atmospheric carbon dioxide concentrations over the past 60 million years. *Nature,* **406,** 695–699.

——, B. E. van Dongen, C. J. Nicholas, R. D. Pancost, S. Schouten, J. M. Singano, and B. S. Wade, 2007: Stable warm tropical climate through the Eocene epoch. *Geology,* **35,** 211–214.

Pierrehumbert, R. T., 1995: Thermostats, radiator fins, and the local runaway greenhouse. *J. Atmos. Sci.,* **52,** 1784–1806.

Ramanathan, V., and W. Collins, 1991: Thermodynamic regulations of ocean warming by cirrus clouds deduced from observations of the 1987 El Niño. *Nature,* **351,** 27–32.

Ramaswamy, V., and Coauthors, 2001: Radiative forcing of climate change. *Climate Change 2001: The Scientific Basis,* J. T. Houghton et al., Eds., Cambridge University Press, 349–416.

Retallack, G. J., 2005: Pedogenic carbonate proxies for amount and seasonality of precipitation in paleosols. *Geology,* **33,** 333–336.

——, 2009: Mechanisms of PETM global change constrained by a new record from central Utah: Comment. *Geology,* **37,** e184–e185.

Reynolds, R. W., and T. M. Smith, 1994: Improved global sea surface temperature analyses using optimum interpolation. *J. Climate,* **7,** 929–948.

Robert, C., and J. P. Kennett, 1994: Antarctic subtropical humid episode at the Paleocene–Eocene boundary: Clay-mineral evidence. *Geology,* **22,** 211–214.

Royer, D. L., R. A. Berner, and J. Park, 2007: Climate sensitivity constrained by CO_2 concentrations over the past 420 million years. *Nature,* **446,** 530–532.

Ruddiman, W. F., and J. E. Kutzbach, 1989: Forcing of late Cenozoic Northern Hemisphere climate by plateau uplift in southern Asia and the American West. *J. Geophys. Res.,* **94,** 18 409–18 427.

Schmidt, G. A., and D. T. Shindell, 2003: Atmospheric composition, radiative forcing, and climate change as a consequence of a massive methane release from gas hydrates. *Paleoceanography,* **18,** 1004, doi:10.1029/2002PA000757.

Schmitz, B., and V. Pujalte, 2007: Abrupt increase in seasonal extreme precipitation at the Paleocene–Eocene boundary. *Geology,* **35,** 215–218.

——, R. P. Speijer, and M. P. Aubry, 1996: Latest Paleocene benthic extinction event on the southern Tethyan shelf (Egypt): Foraminiferal stable isotopic ($\delta^{13}C$, $\delta^{18}O$) records. *Geology,* **24,** 347–350.

Scrutton, C. T., 1978: Periodic growth features in fossil organisms and the length of the day and the month. *Tidal Friction and the Earth's Rotation,* P. Brosche and J. Sündermann, Eds., Springer-Verlag, 154–196.

Seidel, D. J., Q. Fu, W. J. Randel, and T. J. Reichler, 2008: Widening of the tropical belt in a changing climate. *Nature Geosci.,* **1,** 21–24.

Sewall, J. O., and L. C. Sloan, 2006: Come a little bit closer: A high-resolution climate study of the early Paleogene Laramide foreland. *Geology,* **34,** 81–84.

——, ——, M. Huber, and S. Wing, 2000: Climate sensitivity to changes in land surface characteristics. *Global Planet. Change,* **26,** 445–465.

Shackleton, N. J., and J. P. Kennett, 1975: Paleotemperature history of the Cenozoic and the initiation of Antarctic glaciation: Oxygen and carbon isotope analyses in DSDP Sites 277, 279, and 281. *Initial Reports of the Deep Sea Drilling Project,* Vol. 29, J. P. Kennett, and M. R. E. Houtz, Eds., 743–755. [Available online at http://www.deepseadrilling.org/29/volume/dsdp29_17.pdf.]

Shellito, C. J., and L. C. Sloan, 2006: Reconstructing a lost Eocene paradise: Part I. Simulating the change in global floral distribution at the initial Eocene thermal maximum. *Global Planet. Change,* **50,** 1–17.

——, ——, and M. Huber, 2003: Climate model sensitivity to atmospheric CO_2 levels in the early-middle Paleogene. *Palaeogeogr. Palaeoclimatol. Palaeoecol.,* **193,** 113–123.

——, J.-F. Lamarque, and L. C. Sloan, 2009: Early Eocene Arctic climate sensitivity to pCO_2 and basin geography. *Geophys. Res. Lett.,* **36,** L09707, doi:10.1029/2009GL037248.

Sloan, L. C., and E. J. Barron, 1992: Eocene climate model results: Quantitative comparison to paleo-climatic evidence. *Palaeogeogr. Palaeoclimatol. Palaeoecol.,* **93,** 183–202.

——, and D. K. Rea, 1996: Atmospheric carbon dioxide and early Eocene climate: A general circulation modeling sensitivity study. *Palaeogeogr. Palaeoclimatol. Palaeoecol.,* **119,** 275–292.

——, and D. Pollard, 1998: Polar stratospheric clouds: A high-latitude warming mechanism in an ancient greenhouse world. *Geophys. Res. Lett.,* **25,** 3517–3520.

——, and M. Huber, 2001: Eocene oceanic response to orbital forcing on precessional time scales. *Paleoceanography,* **16,** 101–111.

Sluijs, A., and Coauthors, 2006: Subtropical Arctic Ocean temperatures during the Palaeocene/Eocene thermal maximum. *Nature,* **441,** 610–613.

——, and Coauthors, 2007a: Environmental precursors to rapid light carbon injection at the Palaeocene/Eocene boundary. *Nature,* **450,** 1218–1221.

——, G. J. Bowen, H. Brinkhuis, L. J. Lourens, and E. Thomas, 2007b: The Paleocene–Eocene thermal maximum super greenhouse: Biotic and geochemical signatures, age models and mechanisms of global change. *Deep-Time Perspectives on Climate Change: Marrying the Signal from Computer Models and Biological Proxies.* M. Williams et al., Eds., The Micropaleontological Society, 323–349.

——, U. Röhl, S. Schouten, H.-J. Brumsack, F. Sangiorgi, J. S. Sinninghe Damsté, and H. Brinkhuis, 2008a: Arctic late Paleocene–early Eocene paleoenvironments with special emphasis on the Paleocene–Eocene thermal maximum (Lomonosov Ridge, Integrated Ocean Drilling Program Expedition 302). *Paleoceanography,* **23,** PA1S11, doi:10.1029/2007PA001495.

——, and Coauthors, 2008b: Eustatic variations during the Paleocene-Eocene greenhouse world. *Paleoceanography,* **23,** PA4216, doi:10.1029/2008PA001615.

Smith, R. D., and P. R. Gent, 2004: Reference Manual for the Parallel Ocean Program (POP): Ocean component of the Community Climate System Model (CCSM2.0 and CCSM3.0). Los Alamos National Laboratory Tech. Rep. LA-UR-02-2484, 75 pp. [Available online at http://www.ccsm.ucar.edu/models/ccsm3.0/pop/doc/manual.pdf.]

Solomon, S., D. Qin, M. Manning, M. Marquis, K. Averyt, M. M. B. Tignor, H. L. Miller Jr., and Z. Chen, Eds., 2007: *Climate Change 2007: The Physical Science Basis*. Cambridge University Press, 996 pp.

St. John, K., 2008: Cenozoic ice-rafting history of the central Arctic Ocean: Terrigenous sands on the Lomonosov Ridge. *Paleoceanography,* **23,** PA1S05, doi:10.1029/2007PA001483.

Storey, M., R. A. Duncan, and C. C. Swisher III, 2007: Paleocene–Eocene thermal maximum and the opening of the northeast Atlantic. *Science,* **316,** 587–589.

Svensen, H., S. Planke, A. Malthe-Sørenssen, B. Jamtveit, R. Myklebust, T. Rassmussen Eidem, and S. S. Rey, 2004: Release of methane from a volcanic basin as a mechanism for initial Eocene global warming. *Nature,* **429,** 542–545.

Thomas, D. J., T. J. Bralower, and J. C. Zachos, 1999: New evidence for subtropical warming during the late Paleocene thermal maximum: Stable isotopes from Deep Sea Drilling Project Site 527, Walvis Ridge. *Paleoceanography,* **14,** 561–570.

Thomas, E., 2003: Extinction and food at the seafloor: A high-resolution benthic foraminiferal record across the initial Eocene Thermal Maximum, Southern Ocean Site 690. *Causes and Consequences of Globally Warm Climates in the Early Paleogene,* S. L. Wing et al., Eds., The Geological Society of America, 319–332.

——, J. C. Zachos, and T. J. Bralower, 2000: Deep-sea environments on a warm earth: Latest Paleocene–early Eocene. *Warm Climates in Earth History,* B. Huber, K. MacLeod, and S. Wing, Eds., Cambridge University Press, 132–160.

Tilburg, C. E., H. E. Hurlburt, J. J. O'Brien, and J. F. Shriver, 2001: The dynamics of the East Australian Current System: The Tasman Front, the East Auckland Current, and the East Cape Current. *J. Phys. Oceanogr.,* **31,** 2917–2943.

Tripati, A., and H. Elderfield, 2005: Deep-sea temperature and circulation changes at the Paleocene–Eocene Thermal Maximum. *Science,* **308,** 1894–1898.

Vecchi, G. A., and B. J. Soden, 2007: Global warming and the weakening of the tropical circulation. *J. Climate,* **20,** 4316–4340.

Wang, L., P. D'Odorico, S. Manzoni, A. Porporato, and S. Macko, 2009: Soil carbon and nitrogen dynamics in southern African savannas: The effect of vegetation-induced patch-scale heterogeneities and large-scale rainfall gradients. *Climatic Change,* **94,** 63–76.

Washington, W., and C. Parkinson, 2005: *An Introduction to Three-Dimensional Climate Modeling*. 2nd ed. University Science Books, 353 pp.

Weijers, J. W. H., S. Schouten, A. Sluijs, H. Brinkhuis, and J. S. Sinninghe Damsté, 2007: Warm arctic continents during the Paleocene–Eocene thermal maximum. *Earth Planet. Sci. Lett.,* **261,** 230–238; Corrigendum, **268,** 243.

Williams, D. M., J. Harkin, and A. H. N. Rice, 1997: Umbers, ocean crust and the Irish Caledonides: Terrane transpression and the morphology of the Laurentian margin. *J. Geol. Soc. London,* **154,** 829–838.

Wing, S. L., G. J. Harrington, F. A. Smith, J. I. Bloch, D. M. Boyer, and K. H. Freeman, 2005: Transient floral change and rapid global warming at the Paleocene–Eocene boundary. *Science,* **310,** 993–996.

Yapp, C. J., 2004: $Fe(CO_3)OH$ in goethite from a mid-latitude North American Oxisol: Estimate of atmospheric CO_2 concentration in the early Eocene "climatic optimum." *Geochim. Cosmochim. Acta,* **68,** 935–947.

Yeager, S. G., C. A. Shields, W. G. Large, and J. J. Hack, 2006: The low-resolution CCSM3. *J. Climate,* **19,** 2545–2566.

Zachos, J. C., and Coauthors, 2004: *Proceedings of the Ocean Drilling Program, Initial Reports.* Vol. 208, doi:10.2973/odp.proc.ir.208.2004.

——, and Coauthors, 2005: Rapid acidification of the ocean during the Paleocene–Eocene thermal maximum. *Science,* **308,** 1611–1615.

——, S. Schouten, S. Bohaty, T. Quattlebaum, A. Sluijs, H. Brinkhuis, S. J. Gibbs, and T. J. Bralower, 2006: Extreme warming of mid-latitude coastal ocean during the Paleocene–Eocene Thermal Maximum: Inferences from TEX_{86} and isotope data. *Geology,* **34,** 737–740.

——, S. M. Bohaty, C. M. John, H. McCarren, D. C. Kelly, and T. Nielsen, 2007: The Paleocene–Eocene carbon isotope excursion: Constraints from individual shell planktonic foraminifer records. *Philos. Trans. Roy. Soc. London,* **365A,** 1829–1842.

——, G. R. Dickens, and R. E. Zeebe, 2008: An early Cenozoic perspective on greenhouse warming and carbon cycle dynamics. *Nature,* **451,** 279–283.